Pro Gradu

Combined electrical transport and Raman measurements of individual single-walled carbon nanotubes

Olli Herranen

January 26, 2009

UNIVERSITY OF JYVÄSKYLÄ

DEPARTMENT OF PHYSICS

NANOSCIENCE CENTER

Preface

The work reported in this Pro Gradu has been done between November 2007 and August 2008 at Nanoscience Center at the Department of Physics in the University of Jyväskylä.

First, I would like to thank my supervisor Prof. Markus Ahlskog for the interesting research topic. I'd also like to thank Prof. Ahlskog and Dr. Andreas Johansson for excellent guidance throughout the project. Furthermore, I'd like to thank all the people who is or has been working in Molecular Technology group especially Mr. Jaakko Leppäniemi, Mr. Mikael Pajunen, Mr. Jarkko Lievonen. I'd also like to thank the staff of Nanoscience Center for an inspirational surrounding and for many advices and discussions.

Finally, I would like to thank Sanna, Elli and the rest of my family for their support and interest towards this project.

Jyväskylä, January 26, 2009

Olli Herranen

Contents

Introduction

The discovery of carbon nanotubes (CNTs) started a boom of nanoscience research. The boom still continues and more interest in nanotechnology is shown all the time. Carbon nanotubes have many fascinating properties because of their unique 1D structure. They are mechanically very strong and their tensile strength is one of the hardest of all materials. Also their remarkable electrical properties make them very promising candidates for many future applications e.g. field-effect transistors and memory elements. There are still big problems before the final victory of nanotubes such as the characterization of it's structure and properties, synthesis of uniform quality material and making organized structures out of them. Future will show whether these problems can be overcome and whether nanotubes might become a greater discovery than the discovery of the transistor.

The aim of this thesis was to study the structure and the electronic properties of single-walled carbon nanotubes (SWCNTs). We fabricated single nanotube devices on top of a highly doped Si wafer covered by dielectric. The Si wafer was used as a backgate and the ends of the CNTs were connected by electrodes of Pd. We performed both electronic transport and Raman measurements on individual single-walled carbon nanotubes. We especially wanted to study the metallic/semiconducting behavior of the tube with these different techniques. The measurements were consistent and both techniques clearly showed the same type of behaviour in the individual tube. Transport measurements gave additional, detailed information about the performance of the nanotube device. Raman measurements on the other hand offered us a way of trying to do the chiral index assignment for an individual tube and that way determine the structure of the tube.

This project was done in collaboration with Mika Petterson's group from the department of Chemistry of the University of Jyväskylä together with Mr. Jyri Rintala who was responsible for the Raman measurements and their data analysis.

Chapter 1

Carbon nanotubes

1.1 History of carbon nanotubes

Carbon nanotubes have been produced as early as in the middle ages, when Syrian blacksmiths developed the Damascus iron [1]. First images of nanotubes have probably been taken by Radushkevich et al. in 1952 [2]. Their report was written in Russian and didn't get noticed in the scientific community. Also Oberling et al. in 1976 [3] reported to image hollow graphitic cylinders. The new era of carbon-related research began in 1985 when a new allotrope of carbon, fullerenes, was found by Kroto et al. [4]. They vaporized graphite by laser irradiation which led to a forming of C_{60} molecule resembling a football. It was named a buckminsterfullerene. Nowadays the C_{60} molecules are called buckyballs. The main authors of the original paper won a Nobel price of chemistry in 1996 for their work on buckyballs.

At 1991, S. Iijima discovered long tubular carbon molecules using the arc-discharge method [5]. The tubules were observed using a transmission electron microscope (TEM), which revealed that the tubules consisted of consentric honeycomb shells. The tubules were thereon called multi-walled carbon nanotubes (MWCNTs). Soon after that in 1993 single-walled carbon nanotubes were discovered by Iijima et al. [6] and Bethune et al. [7].

The outstanding and unique mechanical and electrical properties of nanotubes make them very interesting for future applications and the discovery of nanotubes was the launch pad for the nanotechonological revolution. Since the first discovery of carbon nanotubes, both scientists and engineers have studied the nanotubes with increasing intensity.

The building block of graphitic materials of all other dimensionalities was found in 2004. It is a 2D sheet of honeycomb lattice [8] and it's called graphene. It can be wrapped up into 0D fullerenes, rolled into 1D nanotubes or stacked into 3D graphite [9]. Theoretically such 2D crystals should be thermodynamically unstable and therefore not exist. This was proved to be wrong when the 2D graphitic sheet was found [9]. Nowadays more interest is focused in researching graphene, which will have very promising

applications in the future [10].

1.2 Synthesis of carbon nanotubes

There are three main methods of fabricating carbon nanotubes: arc-discharge, laser ablation and chemical vapor deposition (CVD). In the arc-discharge method there are two carbon rod electrodes separated by ∼1 mm. The voltage across the electrodes is set to be ∼ 20 V and DC current flowing between electrodes to be 50-120 A. The nanotubes start to form in cathod while the anod is shortened. With the use of catalyst particles, one can both produce SWCNTs and control the diameter distribution of tubes [11]. This method is a simple way to produce bulk amounts of CNT material.

Secon method is laser ablation. In this method laser pulses are used to hit the graphite target. The target also consists of also small amounts of Co-Ni alloy as catalyst. Flowing gas then carries the tubes away from the target to a cooled collector. With this method it is possible to fabricate large amounts of high-quality SWCNTs [11].

The CVD method needs gaseous compound of carbon which is then catalyzed by metallic nanoparticles. This method is nowadays the most important commercial method for SWCNT production. With this method it is easier to control morphology and structure of the produced tubes. Furthermore, it is possible to grow single individual tubes straight on top of the substrate and for example over a slit. There are many different CVD methods and the following five are the most widely used: methane CVD, HiPCO, CO CVD, alcohol CVD and PECVD (plasma-enhanced CVD) [10].

1.3 Applications of carbon nanotubes

The unique 1D sturcture of carbon nanotubes makes them a potential candidate to several different applications. One major field is applications in electronics. CNTs are very promising electronic materials because they can be either metallic or semiconducting and achieve ballistic conduction. Carbon nanotube field-effect transistors are reported to be much better than traditional silicon-based ones [10]. They can be also packed into a smaller space which makes this technology faster than traditional silicon-based technology. Metallic nanotubes can also be used as interconnets. Therefore it is possible to make integrated circuits from them. Carbon nanotubes can be also used as electromechanical memory devices [12], electrostatic discharge (ESD) applications, cooling applications and invisible circuits (thin-film transistors, displays).

Carbon nanotubes can be used in energy applications like in batteries and other energy-storage devices. They can be used in forming a bulk heterojunction in solar cells and utilized in different conjugated polymer matrices with improvement in charge separation and transport [10]. Carbon nanotubes can also be used for mechanical applications. The best known example is the use of CNTs in composites [10]. The

nanotubes are attached to the epoxy which holds the fibers together. This makes the composites stronger yet flexible. There are lots of different applications for nanotubes acting as sensors, in field-emission and lightning applications and biological applications [10].

The wide range of potential applications makes the tubes a fascinating research area. In many of the fields there are still a number of problems to be solved before they are able to make commercial products. One major challenge is the lack of mass production of SWCNTs. For MWCNTs it can be done with but for SWCNTs the fabrication amounts are still measured in gram quantities. There also remain great challenges in applications that need organized nanotube structures. A fast, low-cost technique to assemble a tube with certain (wanted) properties in desired location does not exist [10].

Chapter 2

Physical properties of carbon nanotubes

Graphene is a sheet of carbon atoms that are densely packed in a honeycomb crystal lattice [11]. This lattice is not a Bravais lattice but it can be formed from tetragon Bravais lattice with two atom basis. The unit cell and Brillouin zone of the graphene honeycomb lattice can be seen on fig. 2.1 (a) and (b). The Brilloiuin zone consists of three high symmetry points, Γ, K and M as the center, the corner, and the center of the edge, respectively. The energy dispersion relations are calculated between these symmetry points. There are two inequivalent K-points in graphene Brillouin zone labeled as $K : \left(0, \frac{4\pi}{3a}\right)$ and $K' : \left(0, -\frac{4\pi}{3a}\right)$ so $\vec{K'} = 2\vec{K}$ and the points are connected by the vector $\vec{K}$.

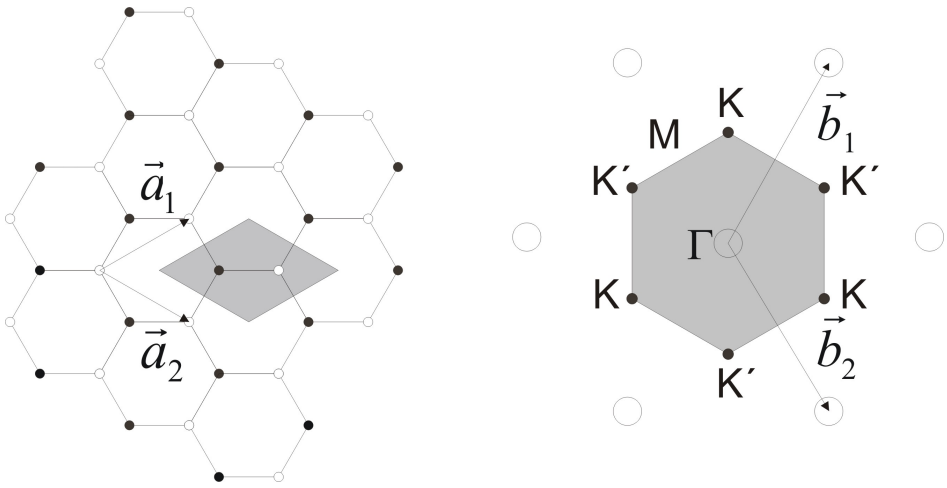

Figure 2.1: a) Graphene honeycomb lattice with two-atom basis (white and black dots represent the two inequivalent carbon atoms), lattice vectors $\vec{a_1}$, $\vec{a_2}$ and the unit cell (gray area). **b)** Reciprocal space, reciprocal lattice vectors $\vec{b_1}$, $\vec{b_2}$ and first Brillouin zone (gray area) of the graphene. Adapted from ref. [11].

Carbon nanotubes are just graphene rolled into a cylindrical form. Therefore, graphene unit vectors $\vec{a_1}, \vec{a_2}$ can be used to describe nanotubes. The nanotube chiral vector or circumferential vector $\vec{C_h}$ can be formed in the use of graphene unit vectors and it describes the structure of nanotube (see fig. 2.2) because the chiral vector is always an integer multiple of lattice vectors $\vec{C_h} = n\vec{a_1} + m\vec{a_2}$. So the whole geometry of the SWNT is determined by a pair of integers (n,m) [13]. The structural parameters of SWNT is descriped on table 2.1. The chiral angle is also the tilt angle of the hexagons with the respect to the tube axis. Nanotubes of the type $(n, 0)(\theta = 0\,^\circ)$ are called zigzag tubes, tubes of type (n, n) are called armchair tubes and tubes type of $((n, m \neq n \neq 0))$ are called chiral tubes.

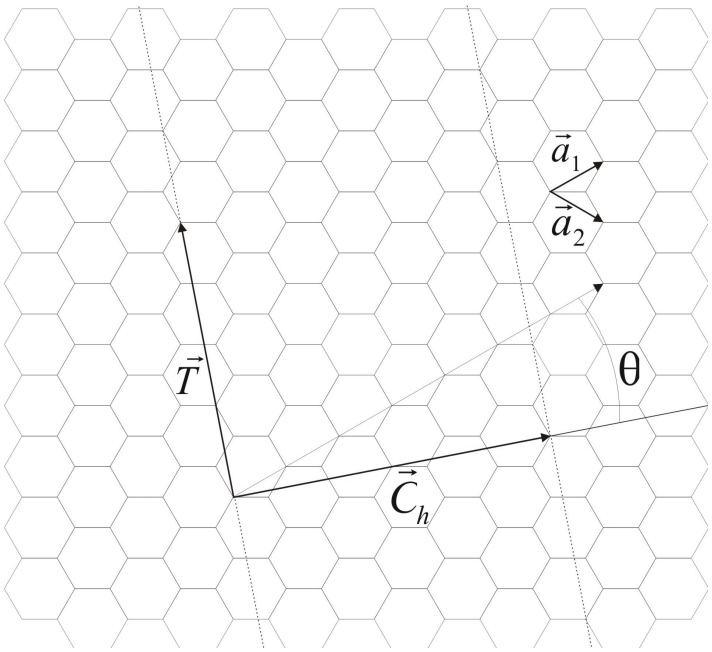

Figure 2.2: Graphene honeycomb lattice with lattice vectors $\vec{a_1}$ and $\vec{a_2}$. The chiral vector $\vec{C_h}$ represents a possible wrapping of the graphene sheet into a tubular form. The direction perpendicular to $\vec{C_h}$ is the tube axis. Adapted from ref. [13].

Table 2.1: Structural parameters for a (n,m) nanotube. Adapted from ref [13]

Symbol	Name	Formula	Values
a	lattice constant	$a = \sqrt{3}a_{cc} \approx 2.46$ Å	$a_{cc} \approx 1.42$ Å
$\vec{a_1}$, $\vec{a_2}$	basis vectors	$\left(\frac{\sqrt{3}}{2}; \frac{1}{2}\right) a$, $\left(\frac{\sqrt{3}}{2}; -\frac{1}{2}\right) a$	
$\vec{b_1}$, $\vec{b_2}$	reciprocal-lattice vectors	$\left(\frac{1}{\sqrt{3}}; 1\right) \frac{2\pi}{a}$, $\left(\frac{1}{\sqrt{3}}; -1\right) \frac{2\pi}{a}$	
$\vec{C_h}$	chiral vector	$\vec{C_h} = n\vec{a_1} + m\vec{a_2} \equiv (n, m)$	$(0 \leq \lvert m \rvert \leq n)$
d_t	tube diameter	$d_t = \frac{\lvert\vec{C_h}\rvert}{\pi} = \frac{a}{\pi}\sqrt{n^2 + nm + m^2}$	
θ	chiral angle	$\sin\theta = \frac{\sqrt{3}m}{2\sqrt{n^2+nm+m^2}}$	$0 \leq \lvert\theta\rvert \leq \frac{\pi}{6}$
		$\cos\theta = \frac{2n+m}{2\sqrt{n^2+nm+m^2}}$	$\tan\theta = \frac{\sqrt{3}m}{2n+m}$
$\vec{T}$	translational vector	$\vec{T} = t_1\vec{a_1} + t_2\vec{a_2} \equiv (t_1, t_2)$	$\gcd(t_1, t_2)$
		$t_1 = \frac{2m+n}{N_R}$, $t_2 = -\frac{2n+m}{N_R}$	$N_R = \gcd(2m + n, 2n + m)$
N_C	number of C atoms per unit cell	$N_C = \frac{4(n^2+nm+m^2)}{N_R}$	

2.1 Electronic properties of carbon nanotubes

To obtain the electronic properties of carbon nanotubes we have to understand the properties of graphene first. Graphene exhibits planar sp^2 hybridization. Carbon has four valence orbitals: $2s$, $2p_x$, $2p_y$ and $2p_z$ orbitals. Among these orbitals the $(s,\ p_x,\ p_y)$ orbitals combine and form bonding σ and antibonding σ^* orbitals. The σ bonds are strong covalent bonds with large energy gap between the states. Therefore they don't play a role on graphene's electronic properties and are often neglected. They however determine the mechanical properties of graphene sheet. The remaining p_z orbital, pointing out of the graphene sheet cannot couple with the σ states. Instead it can form delocalized orbitals which have bonding π and antibonding π^* orbitals close to the fermi energy E_F. The last valence electron occupies the π orbital and takes part of the electrical conduction of the tube [13].

The energy dispersion relation of graphene can be derived from tight-binding model

and it is

$$E^{\pm}(k_x, k_y) = \pm\gamma_0\sqrt{1 + 4\cos\frac{\sqrt{3}k_x a}{2}\cos\frac{k_y a}{2} + 4\cos^2\frac{k_y a}{2}}, \tag{2.1}$$

where γ_0 is the transfer integral between first-neighbor π orbitals. So, there are two energy branches and they cross at the points where $E = 0$. The crossing points lie at vertices of the first Brillouin zone in the K points. Because there is no energy gap between the bands in K-points, graphene is called zero bandgap semiconductor. Graphene's unit cell consists of two carbon atoms (see fig. 2.1) both having one free electron. These electrons occupy the lower branch leaving the higher branch empty so that the bands indeed are the valence and conduction bands.

When the graphene sheet is rolled on the tube, the periodic boundary conditions along the tube's circumferential direction leads to quantization of the allowed wave vectors around the tube circumference. The basic idea for this electronic zone-folding (EZF) approximation is that the electronic band stucture of a certain nanotube is given by superposition of the graphene energy bands along the corresponding allowed $\vec{k}$ lines. The periodic boundary conditions of the wavefunction are:

$$\Psi_{\vec{k}}(\vec{r} + \vec{C_h}) = e^{i\vec{k}\cdot\vec{C_h}}\Psi_{\vec{k}}(\vec{r}) = \Psi_{\vec{k}}(\vec{r}), \tag{2.2}$$

where $\vec{k}$ and $\vec{r}$ are on the surface on nanotube. Near fermi surface, that is, in the vicinity of K points, we can make an analysis $\vec{k} = \vec{K} + \delta\vec{k}$ ($\delta\vec{k}$ is small). Noticing the boundary conditions we get that $\delta\vec{k}\cdot\vec{C_h} = 2\pi q$ (q is integer). Therefore there is only set of parallel lines through BZ as shown in fig. 2.3 (a). Each line corresponds to a different value of q and for each line we can write a one-dimensional dispersion relation $E_q(\vec{k})$. If at least one k-line crosses the K point the tube is metallic and if none of the lines cross then there will be an energy gap between the valence and conduction bands and the tube is semiconducting. The Brillouin zone of nanotube is one dimensional and the zone edges are usually labeled X, $\vec{X} = \pm(\pi/T)\vec{\kappa}_{||}$, where $\vec{\kappa}_{||}$ is the basis vector along $\vec{T}$ direction. Therefore, the nanotube band structure is represented along the ΓX direction.

The dispersion relation for metallic nanotubes becomes linear near fermi level and it is [13]

$$E^{\pm}(\delta\vec{k}) \approx \pm\frac{\sqrt{3}a}{2}\gamma_0||\delta\vec{k}||. \tag{2.3}$$

For semiconducting tubes we get with the same treatment that dispersion relation near Fermi energy is

$$E_q^{\pm}(k_{||}) \approx \frac{\sqrt{3}a}{2}\gamma_0\sqrt{\left(\frac{2\pi}{|\vec{C_h}|}\right)^2\left(q \pm \frac{1}{3}\right)^2 + k_{||}^2}, \tag{2.4}$$

where integer q counts the available bands and $k_{||}$ is the part of the wavevector that describes the states within a given subband. From equation (2.4) we get the band gap

at the fermi level

$$\Delta E_g = E_0^+(0) - E_0^-(0) = \frac{2\pi a\gamma_0}{\sqrt{3}|\vec{C_h}|} = \frac{2a\gamma_0}{\sqrt{3}d_t} \approx \frac{0,8\ eV\ nm}{d_t}, \tag{2.5}$$

when assuming that the transfer integral $\gamma_0 = 2,9$ eV. We can clearly see that the energy gap of the nanotube is inversely proportional to its diameter. Armchair tubes are always metallic and chiral tubes are metallic if $(n-m) = 3q$ and semiconducting if $(n-m) = 3q \pm 1$. From these we can estimate that roughly $\frac{1}{3}$ of the tubes are metallic and rest are semiconducting. With curvature effects included, group symmetry can be used to show that only armchair tubes are truly metallic. All other tubes satisfying metallic condition are only quasi-metallic with small band gap [14]. We can modify the equation (2.5) in new form determining the effective mass of the charge carriers. That's an important quantity when studying the transport properties of the tube. The relation is

$$E_0^{\pm} = \pm\sqrt{(m^* v_F^2)^2 + (\hbar k_{||} v_F)^2}, \tag{2.6}$$

where effective mass m^* is defined $m^* = 2\pi\hbar/3|C_h|v_F$ and v_F is the fermi velocity, $v_F = \sqrt{3}\gamma_0/2\hbar \approx 8 \cdot 10^5$m/s for $\gamma_0 = 2,9$ eV [13].

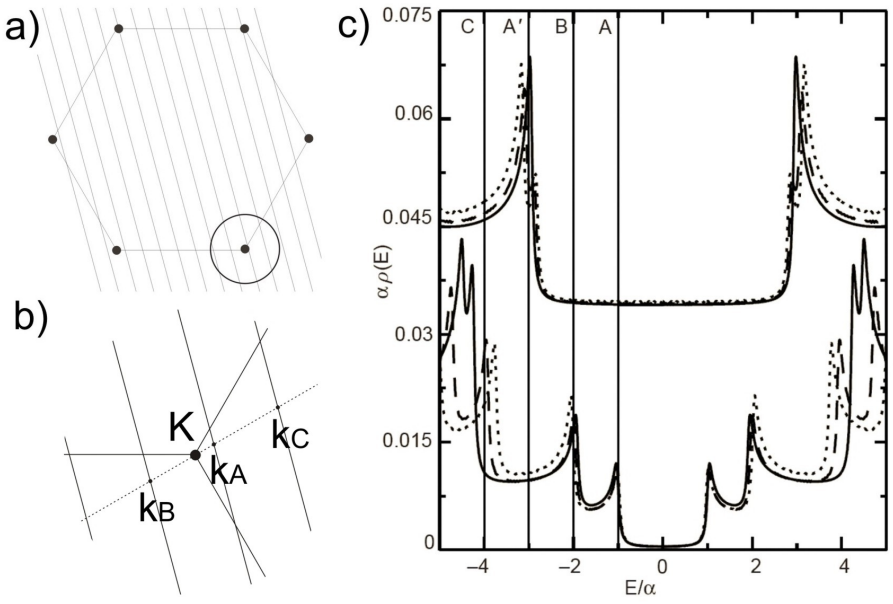

Figure 2.3: (a) Graphene Brillouin zone and allowed k-states in SWCNT (parallel lines). (b) Expanded depiction of allowed states near K point. k_A, k_B, k_C are special points closest to K point in the nearest allowed k-lines. Dashed line is the direction of the chiral vector $\vec{C_h}$. (c) Density of states per carbon atom. Points A, B and C refers to the points in fig. (b). Point A' is the first singularity of metallic tube predicted by theory. Adapted from ref. [16].

The density of states (DOS) $D(E) = \Delta N/\Delta E$ represents the number of available states for a given energy interval. The shape of DOS depends dramatically on dimen-

sionality. In one dimensonal systems the DOS is inversely proportional to the square root of the energy [15]. The DOS diverges close to band extrema and these peaks are called Van Hove singularities (VHSs). Nanotubes are quasi-1D objects and the DOS is bit different than in usual 1D objects. The DOS for nanotubes is

$$D(E) = \frac{2a}{\pi\gamma_0|\vec{C_g}|}\sum_{q=1}^{2n}\sum_{s=\pm}\frac{|E_q^s(k)|}{\sqrt{(E_q^s)^2(k)-\epsilon_{qs}^2}}, \tag{2.7}$$

where E_q^s is the energy of the certain branch at given k-line and ϵ_{qs} the energy position of VHSs ($|\epsilon_{qs}| = \pi\gamma_0 a_{cc}|3q-n+m|/|C_h|$) [13]. Compared to graphene's density of states, nanotube has several peaks on it occuring the quantization of the tube in circumferential direction as seen in figure 2.3 (c) and the position of the VHSs can be derived from the dispersion relations. For metallic tubes there is no band gap at fermi energy and the density of states is constant [14]:

$$D(E_F) = \frac{2\sqrt{3}a_{cc}}{\pi\gamma_0|\vec{C_h}|}. \tag{2.8}$$

For semiconducting tubes there is always a band gap ($E_g = E_c - E_v$) which automatically means that $D(E_F) = 0$. The electronic excitations between the VHSs depends strongly on nanotube diameter and they also have much weaker dependence on chiral angle. This dependence on chiral angle is caused because of the three-fold symmetry of the electronic dispersion relations near K-point. Away from K-points the energy bands exhibit trigonal warping effect which is responsible for the unique energy bands is SWCNTs. This effect causes a spread of the interband energies $E_{ii}(d_t)$ for the tubes having a same diameter.

2.2 Transport properties of carbon nanotubes

The conductance of quasi-1D system is given by Landauer formula [17]:

$$G(E) = \frac{2e^2}{h} M(E)T, \tag{2.9}$$

where M(E) is the number of subbands contributing to charge transfer and T is the average transmission propability of each subband. In mesoscopic systems there can be determined three kinds of characteristic lengths of the system: the mean free path l_m, the Fermi wavelength λ_F and the phase relaxation length l_ϕ [18]. Mean free path describes the average length that electrons travel before scattering. The Fermi wavelength is the de Broglie wavelength of electrons at Fermi energy and the phase-relaxation length is the average length where electon retains it coherence as a wave. Elastic scattering of electrons doesn't contribute for l_ϕ, only for l_m but inelastic scattering contributes both of them. In the case of electron-electron scattering between two valence electrons the contribution is only for l_ϕ. Only electrons that are near Fermi energy contribute in transport properties so the lengths l_m and l_ϕ are scaled by the Fermi velocity as follows [18]

$$l_m = v_F \tau_m \qquad \& \qquad l_\phi = v_F \tau_\phi, \tag{2.10}$$

where τ_m is the momentum relaxation time and τ_ϕ the phase relaxation time. The times correspond in the overall changes of phase and momentum in the system, not a single scattering event. This means for example that changes in momentum reaches $\hbar k_F$ and phase π, respectively. There are three different transport regimes: ballistic, diffusive and classical. The relationship between the characteristic lengths determines then the transport regime. The conductance is ballistic when the 1D channel length between contacts is smaller than mean free path and phase relaxation length of the channel [18]. It means that there are no scattering centers in the channel and transmission probability T becomes one. The only resistance in the ballistic case comes from contacts. If the contacts are ideal (Ohmic), reflectionless, the resistance reaches the quantized value. However, in general there is also scattering at the channel. Then the resistance of the device is $R_c + R_t$, where R_c is the contact resistance and R_t is the resistance of the channel. The surrounding enviroment then also affects the conduction especially at the high electric field due to reduced dimensionality for thermal conduction and phonon relaxation.

Carbon nanotubes are reported to be 1D ballistic conductors [19], [20], [21]. In metallic nanotubes there are two conduction channels because two subbands cross at Fermi energy [22]. The theoretical maximum conductance for such device can be obtained from the equation (2.9) by setting $T = 1$ & $M = 2$:

$$G_q = \frac{4e^2}{h} = 2G_0 \approx 1.549 \cdot 10^{-4} S,$$

where G_0 is the quantum conductance. Also semiconducting nanotubes can be ballistic conductors so that both the valence and the conduction band act as a conduction channel. In reality the there will always be backscattering in the contact interface which leads that $T < 1$ and so metal electrode-nanotube contact has a big influence on the transport properties of the tube [13]. Metallic nanotubes can get really close to the conductance maximum with ideal Ohmic contacts [19], [20]. In the case of metal-semiconducting nanotube contact a Schottky barrier is formed in the interface [21], [23]. The role of contacts and the channel itself will be discussed more detailed in the following sections.

2.2.1 Contact resistance

There are mainly two types of barriers that can be formed in the metal-CNT interface, which increase the value of the contact resistance from the ideal G_q value. One barrier is called Schottky barrier. It is a potential barrier that is formed at a metal-semiconductor junction. The properties of the barrier will depend on the band alignment at the interface. The barrier height can be estimated as the work functions of the metal and nanotube. The work function is the potential energy difference of electron between vacuum level and Fermi level. On semiconcuctors the work function is usually defined by means of electron affinity χ which is the energy difference between vacuum level and conduction band. Then the work function can be expressed as a sum of electron affinity and half of the bandgap energy [24].

When the metal and semiconductor are brought into planar contact the Fermi levels of the materials are balanced at the thermal equilibrium. This causes the bands of semiconductor to bend and the barrier is formed in the interface. Even though the work functions were same for both materials, it is hard to form flat contact at the interface. The reason is that in the semiconductor side of the interface so called MIGS are formed (metal induced gap states) [25], [26]. States that are in the semiconductor gap decay expontentially into semiconductor. These MIGS produce planar dipoles that pins down the Schottky barrier height and make it nearly independent of the contact metal work function [26]. The occupancy of the states depends on the position of the Fermi level at the semiconductor. The barrier for the electrons, for example, can be then simply estimated as [25]

$$\Phi_b = E_C - E_N, \tag{2.11}$$

where E_C is the energy of the conduction band and E_N the energy of the charge neutrality level. The charge neutrality level is the energy level where the gap states of the semiconductor surface change from valence to conduction-type character.

The reduced dimensionality of the CNT makes the interface a bit different than in bulk samples. The n-type barrier for electron injection is formed between the metal Fermi level and conduction band of CNT and p-type barrier for hole injection between

metal Fermi level and valence band of CNT as shown in figure 2.4 (a):

$$\phi_{SB}^{n} = \phi_M - \phi_{CNT} + \frac{1}{2}E_g = \phi_M - \chi, \tag{2.12}$$

$$\phi_{SB}^{p} = \phi_{CNT} + \frac{1}{2}E_g - \phi_M = \chi + E_g - \phi_M, \tag{2.13}$$

where ϕ_M is the work function of the metal and ϕ_{CNT} the work function of the nanotube. The work function of the nanotube is defined as $\phi_{CNT} = \chi + \frac{1}{2}E_g$.

Because the contact area between the metal and the tube is small, the MIGS induced dipole is localized near the interface. The contact then determines the Fermi level pinning at the interface. When the nanotube is connected to the metal with the end contacts the bonds between the tube and metal are covalent. The charge neutrality level of the tube and Fermi level of the metal will meet each other at the interface. For the intrinsic semiconducting nanotubes the charge neutrality level lies in the middle of the semiconducting gap because the DOS of the CNT is symmetric around Fermi energy. This causes the bending of the bands. The work function of metal and the bandgap of CNT determines in which region the contact will be. In the case of CNTs whose work functions have reported to be (4.7-4.9) eV [27] and high work function metal like Palladium ($\phi_{Pd} = 5.1$ eV) p-type contacts are formed (fig. 2.4 (b)) and metals with low work function like Aluminium ($\phi_{Al} = 4.1$ eV) the contacts are more n-type (fig. 2.4 (c)). It has been reported that ohmic contacts (zero Schottky barrier) to the valence band have been formed with Palladium and CNTs whose diameter is $\sim 1,6$ nm ($E_g \sim 0,6$ eV) [21].

The barrier thickness determines the performance of the junction because the current through the barrier is based on thermally assisted quantum mechanical tunneling. The thickness of the barrier can be modulated with gate voltage. The tunneling current depends exponentially from the barrier thickness for fixed V_{DS} [24].

The role of the contact has been reported to have great influence to the behaviour of the junction [28]. Besides the geometry of the contact and the work function of the metal also the wetting properties of the metal have big influence [21], [22]. The ideal case would be to have metal whose wetting properties are good and work function is at the same value as valence or conduction band of the tube. Then the barrier would not affect the charge injection so much and the ON-state current would not be affected by the barrier.

Other barrier is created by an imperfect interface between the metal and nanotube. It is a pure tunneling barrier and the resistance of this barrier is a function of the interface's cleanliness and the overlap of the metal-CNT electronic states [10]. The metal wetting properties have a key role when forming bonds to CNT. Metals such Pd forms good contacts to CNTs but then other metals with same work function (like Pt) does not make such a good contacts [26].

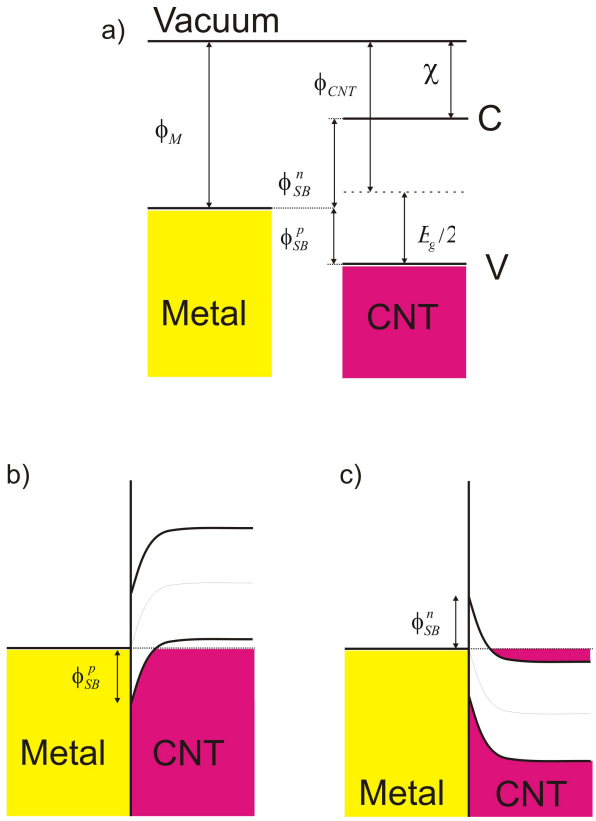

Figure 2.4: Schottky barrier at metal-nanotube interface. a) The energy levels for metal and nanotube before alingment depicting the relation between barrier heights for hole and electron injection (ϕ^p_{SB} & ϕ^n_{SB}) and the work function of metal (ϕ_M) and tube ϕ_{CNT}. b) Band alignment in the the case of high work function metal, where the contact will be p-type. c) Band alignment in the case of low work function metal. Then the contact will be n-type. Adapted from the ref. [10].

2.2.2 Resistance of the channel

Additional resistance in the nanotube itself can occur from many different scattering processes. One major scattering mechanism is electron-phonon scattering especially at room temperature for metallic tubes. Scattering by acoustic phonons dominates at small bias voltages, whereas scattering by optical and zone-boundary phonons at large bias voltages [10]. The effects of the enviroment have been demonstrated to affect to the transport of the tube significantly (see fig. 2.5). The transport and phonon scattering is completely different in suspended tubes compared to the tubes on the substrate [29]. The current saturates because electron emits a phonon as soon as its energy has reached the optical phonon energy and this happens very fast. The excess energy created by the phonon can be remarkable and this heats the tube. Also the created phonons can scatter even more electrons which leads to greater resistance. Even negative differential conductance can be seen in the suspended tubes as shown in figure

2.5. Tubes that are on the substrate have more interaction with the substrate and that leads to greater heat dissipation and relaxation of the optical phonons emitted through electron scattering. The phonon scattering also affects the semiconducting tubes and the tube ON-state resistance has been reported to grow linearly with temperature, which implies to scattering of acoustic phonons [30].

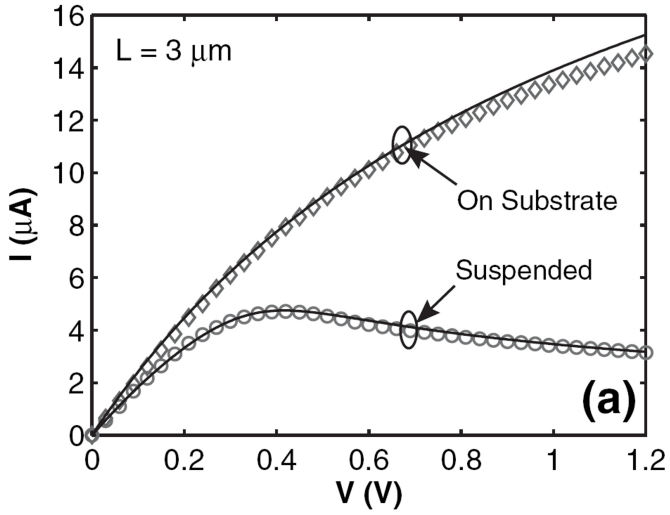

Figure 2.5: I-V characteristic of same length suspended and non-suspended portions of metallic SWCNT at room temperature in vacuum. Adapted from ref. [29].

There are also many sources of disorder such as localized lattice defects [31], electrostatic potential fluctuations and mechanical deformations [32], [33] that affect the scattering processes. The effects of disorder for clean nanotubes become dominant at low temperatures and these effects can be determined by extracting the mean free path of nanotube. The mean free paths of both metallic and semiconducting nanotubes have been reported to be several microns in low T [34], [35].

There are two different backscattering processes in which the disorder play an important role. The backscattering can be between two different branches (originating from K and K' points) or within the same branch. In the first process there is a big momentum transfer and therefore only disorders that are in atomic scale can occur. The other process requires only small momentum transfer and is caused by long-range disorder. For metallic tubes there are only short-range disorder present but for semiconducting tubes both processes are present [10].

2.2.3 Quantum effects

Quantum effects become relevant at low temperature when thermal energy is reduced enough. Especially in reduced dimensionality these effects are more visible because of

the larger energy scales. Quantum effects include for example the Coulomb blockade of conduction, interference effects, Kondo effects [10].

When the contact resistance between the tube and electrodes is large, Coulomb blockade effect arise. It happens when the total capacitance of a metallic island becomes small enough so that the energy required to add an electron to the island becomes larger than the thermal energy [13]. The condition is therefore

$$E_c = \frac{e^2}{2C} > k_B T = E_T. \tag{2.14}$$

It can happen in nanotubes when conducting island is weakly coupled to source and drain electrodes through tunnel barriers whose resistance is larger than h/e^2. Also only a fraction of the tube can act as a conducting island. This basically means that either the whole tube is acting as a quantum dot or only a part of it.

When the contact resistance is very small so that the contacts are nearly perfect, Fabry-Pérot interference can happen. Then the nanotubes act as coherent electron waveguides. Resonant cavity is then formed between the two electrode-nanotube interfaces [36]. Interference effects where the wave function of the charge carrier maintains its phase coherence are called weak localization. The condition is $l_m << l_\phi$ what means that electrons can interfere while scattering. The transport is then rather diffusive than ballistic and the correction term for the conductance deduced from the weak localization is [13]

$$\delta G_{WL}(E) = \frac{2e^2}{h} - G(E). \tag{2.15}$$

The Kondo effects on the other hand are due to the hybridization of localized spin with a continuum of conduction electrons below characteristic temperature [10].

2.3 Vibrational properties of carbon nanotubes

As electronic properties of nanotubes, vibrational properties can also be explained in the use of graphene. The differences between graphene and nanotubes can be explained in the terms of curvature and confinement (quantization of electronic momentum). But it is not as straightforward to get phonon dispersions as electron dispersions. Atomic vibrations are partially screened by electrons. This screening can change the vibrations associated with certain q-point in the Brillouin zone. This anomalous behavior of the phonon dispersions is called Kohn anomaly [37]. Kohn anomalies occur only for $\vec{q}$ so that there are two electronic states on the Fermi surface $\vec{k_1}$ and $\vec{k_2} = \vec{k_1} + \vec{q}$. In Graphene there are two scattering process for electrons. The electrons can scatter within the same K or K' point by the phonon modes around Γ point. This process is called intravalley scattering. The other option for electrons is to scatter between different K and K' points by the phonon modes near the K or K' point and that process is called intervalley scattering [38]. Therefore Kohn anomalies in graphene can happen only when $\vec{q} = \vec{\Gamma}$ or $\vec{q} = \vec{K}$. The following sections explains briefly optical phonons in graphene and carbon nanotubes. The EPC affecting optical phonons in graphene and nanotubes can be studied in the use of density functional theory (DFT) which is explained more detailed in references [39]– [41].

2.3.1 Optical phonons in graphene

The dispersion relations for highest optical branches show that there are discontinuity in frequency derivative at Γ and K because of the metallic nature of graphene. To understand this behaviour near fermi surface we have to solve the dynamical matrix element of electron-phonon coupling (EPC). The EPC of graphene is defined different ways [39] and following expressions can be obtained:

$$|D|^2 = \frac{9}{2\eta^2}, \tag{2.16}$$

where η is the derivative of the hopping integral with respect to C-C distance,

$$|g| = |D|\sqrt{\frac{\hbar}{2M\omega_q}}, \tag{2.17}$$

where g is the phonon charasteristic length, M the atomic mass and ω_q frequency of the phonon. Expressing the matrix adiabatic and describing the electron-phonon coupling with a first neighbour tight-binding model, it's possible to derive analytical expression of Kohn anomalies in graphene [40]. Let's define

$$\langle D^2_{\Gamma/K} \rangle_F = \frac{\sum_{i,j}^{\pi} \mid D_{\vec{K}i,\vec{K}j} \mid^2}{4}, \tag{2.18}$$

where sum is over the two degenerate π bands at the Fermi level and $D_{(\vec{k}+\vec{q})i,\vec{k}j} = \langle \vec{k}+\vec{q}, i \mid \Delta V_q \mid \vec{k}, j \rangle$ is the EPC matrix element where $\mid \vec{k}, i\rangle$ is the electronic Bloch eigenstate of wavevector $\vec{k}$ in band i with energy $\epsilon_{k,i}$ and occupation $f_{k,i}$ given by the Fermi-Dirac distribution, ΔV_q is the derivative of the vector potential with respect to a displacement along the phonon normal coordinate. The dispersion relation near Γ point is [41]

$$\hbar\omega_{\vec{q}} = \alpha_\Gamma q + \hbar\omega_\Gamma + \vartheta(q^2), \tag{2.19}$$

where α_Γ is the slope of the curve near Γ. The relation is similar also near K point:

$$\hbar\omega_{\vec{K}+\vec{q'}} = \alpha_K q' + \hbar\omega_K + \vartheta(q'^2). \tag{2.20}$$

The slopes of these relations can be calculated in the use density functional perturbation theory [39] and they are proportional to the square of EPC and inversely proportional to the fermi velocity v_F:

$$\alpha_\Gamma^{LO} = \frac{\sqrt{3}\hbar a^2}{8M\omega_\Gamma\beta}\langle D_\Gamma^2\rangle_F \tag{2.21}$$

and

$$\alpha_K^{TO} = \frac{\sqrt{3}\hbar a^2}{8M\omega_K\beta}\langle D_K^2\rangle_F, \tag{2.22}$$

where $\beta = \hbar v_F$ is the slope of the electron bands near ϵ_F, M is the carbon atomic mass, ω_Γ is the frequency of the E_{2g} phonon and ω_K is the frequency of the A_1' phonon. The dispersion relations of highest optical branches are shown in fig. 2.6. It's clearly seen that at the points Γ and K there is a Kohn anomaly caused by EPC. So the optical phonons of graphene which have considerable EPC are the E_{2g} phonon at Γ and the A_1' phonon at K.

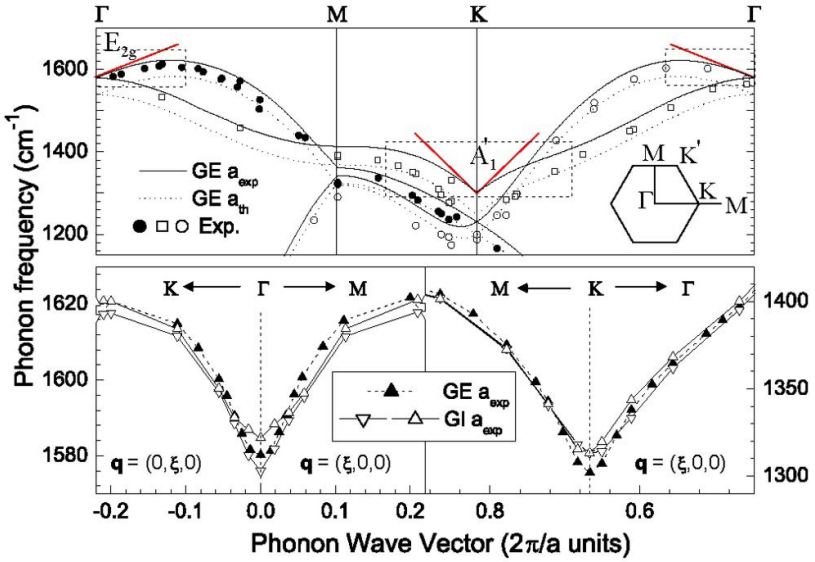

Figure 2.6: The phonon dispersion of graphene calculated at experimental and equilibrium lattice spacings. Red straight line are the calculated slopes. Points are the experimental data. Adapted from the ref. [41].

2.3.2 Optical phonons in SWCNTs

The electron-phonon coupling (EPC) in nanotube is related to that of graphene as follows

$$|D^2| = \frac{a^2\sqrt{3}}{2T\pi d_t}|\tilde{D}^2|, \tag{2.23}$$

where D is the EPC of tube and $\tilde{D}$ EPC of the graphene [39]. The phonon frequencies in SWCNTs can be calculated using zone foldinq technique. The direct phonon zone folding (PZF) cannot be used because KAs affect differently in graphene and metallic nanotubes. In semiconducting nanotubes there is no KAs at all. Instead the phonon frequencies can be calculated by the use of electronic zone folding discussed in section 2.1. This can be done by calculating the nanotube dynamical matrices in the use of density functional perturbation theory (DFPT). The dynamical matrix projected on phonon normal coordinate is defined as

$$\begin{aligned}\Theta_q =& \frac{2T}{2\pi}\sum_{m,n}\int_{BZ}\frac{\mid D_{(\vec{k}+\vec{q})n,\vec{k}m}\mid^2 (f_{\vec{k}m} - f_{(\vec{k}+\vec{q})n})}{\epsilon_{\vec{k}m} - \epsilon_{(\vec{k}+\vec{q})n} + \hbar\omega_{\vec{q}} + i\gamma}dk \\ &- \int \Delta n_q^*(\vec{r})K(\vec{r},\vec{r'})\Delta n_q(\vec{r'})d\vec{r}d\vec{r'} + \int n(\vec{r})\Delta^2 V^b(\vec{r})d\vec{r},\end{aligned} \tag{2.24}$$

where $2\pi/T$ is the length of the tube's BZ, $\sum_{m,n}$ is a sum on all possible electronic transitions, $\int_{BZ} dk$ an integral over the tube BZ, $\epsilon_{k,n}$ the energy of the electronic Bloch eigenstate with wave vector k and band index n, γ small real constant, $n(\vec{r})$ the

charge density and $\Delta^2 V^b(\vec{r})$ second derivative of the purely ionic potential. $K(\vec{r},\vec{r'}) = \delta^2 E_{Hxc}(n)/\delta n(\vec{r})\delta n(\vec{r'})$, where E_{Hxc} is the Hartree and exchange-correlation functional. $D_{(k+qn),km}$ is the electron-phonon coupling matrix element as defined in equation (2.18) [39]. So the phonon is described here as a time-dependent perturbation of the system. The phonon frequencies are simply

$$\omega_q = Re\left\{\sqrt{\frac{\Theta_q}{M}}\right\}. \tag{2.25}$$

The static approximation neglects the dynamic effects and the matrix becomes

$$\begin{aligned}\Theta_q =& \frac{2T}{2\pi}\sum_{m,n}\int_{BZ}\frac{\mid D_{(\vec{k}+\vec{q})n,\vec{k}m}\mid^2 (f_{\vec{k}m} - f_{(\vec{k}+\vec{q})n})}{\epsilon_{\vec{k}m} - \epsilon_{(\vec{k}+\vec{q})n}}dk \\ &- \int \Delta n_q^*(\vec{r})K(\vec{r},\vec{r'})\Delta n_q(\vec{r'})d\vec{r}d\vec{r'} + \int n(\vec{r})\Delta^2 V^b(\vec{r})d\vec{r}.\end{aligned} \tag{2.26}$$

This approximation is real and the frequencies are

$$\omega_q = \sqrt{\frac{\Theta_q}{M}}. \tag{2.27}$$

There are singularities in phonon dispersions for states close to Fermi energy because the denominator of equation (2.26) goes to zero. These singularities are also present in the real part of equation (2.24) when phonon's energy matches an electronic transition. The dynamical matrix can be divided into an analytic and a non-analytic component in order to study such singularities:

$$\Theta_q = \Theta_q^{an} + \tilde{\Theta}_q. \tag{2.28}$$

The non-analytic part of the matrix is

$$\tilde{\Theta}_q = \frac{2A_{\Gamma/K}T}{2\pi}\sum_{m,n}\int_{-\bar{k}}^{\bar{k}}\frac{\mid D_{(\vec{K}+\vec{k'}+\vec{q})n,(\vec{K}+\vec{k'})m}\mid^2 (f_{(\vec{K}+\vec{k'})m} - f_{(\vec{K}+\vec{k'}+\vec{q})n})}{\epsilon_{(\vec{K}+\vec{k'})m} - \epsilon_{(\vec{K}+\vec{k'}+\vec{q})n} + \hbar\omega_{\vec{q}} + i\gamma}dk, \tag{2.29}$$

where $\bar{k}$ has small but finite value and $A_{\Gamma/K}$ accounts for the number of processes satisfying $2q = K$ ($A_\Gamma = 2$, A_K=1). The static approximation of this is naturally

$$\tilde{\Theta}_q = \frac{2A_{\Gamma/K}T}{2\pi}\sum_{m,n}\int_{-\bar{k}}^{\bar{k}}\frac{\mid D_{(\vec{K}+\vec{k'}+\vec{q})n,(\vec{K}+\vec{k'})m}\mid^2 (f_{(\vec{K}+\vec{k'})m} - f_{(\vec{K}+\vec{k'}+\vec{q})n})}{\epsilon_{(\vec{K}+\vec{k'})m} - \epsilon_{(\vec{K}+\vec{k'}+\vec{q})n}}dk. \tag{2.30}$$

The doubly degenerate $\Gamma - E_{2g}$ phonon of graphene splits into a lognitudal optical (LO) and transverse optical (TO) modes for both metallic and semiconducting tubes because of the confinement effects. Also for metallic tubes $\omega_{TO}^M > \omega_{LO}^M$ but for semiconducting tubes $\omega_{LO}^{SC} > \omega_{TO}^{SC}$. The reason is that EPC at Γ has a finite value for LO modes and null for TO modes. Therefore, from equation (2.30) can be obtained that

$\omega_{TO}^{graph} = \omega_{TO}^{SC} = \omega_{TO}^{M}$. The physical observable determining the EPC in SWCNTs is EPC times the density of states (DOS). The DOS is null for semiconducting tubes close to Fermi energy and for metallic tubes it's constant. In graphene the DOS is null at Fermi energy and increases linearly when $\epsilon \neq \epsilon_F$, so therefore we can write for DOS $g(E)$ that $g_{\epsilon_F}^{SC} < g_{\epsilon_F}^{graph} < g_{\epsilon_F}^{M}$. Again from equation (2.30) we get $\omega_{LO}^{M} < \omega_{LO}^{graph} < \omega_{LO}^{SC}$. Because in graphene $\omega_{LO}^{graph} = \omega_{TO}^{graph}$ we eventually get that $\omega_{LO}^{SC} > \omega_{TO}^{SC}$ and $\omega_{LO}^{M} < \omega_{TO}^{M}$.

In zero temperature the static approximation of the non-analytical matrix $\tilde{\Theta}_q$ can be derived from equation (2.30) and it depends logarithmically on q for E_{2g}-Γ LO-mode and for A_1'-K mode. For Γ TO-mode the matrix is constant:

$$\tilde{\Theta}_{LO/K} = \frac{A_{\Gamma/K}\sqrt{3}a^2\langle D_{\Gamma/K}^2\rangle_F}{\pi^2\beta d}\ln q + C'_{LO/K}, \tag{2.31}$$

$$\tilde{\Theta}_{TO} = -\frac{A_{\Gamma}\sqrt{3}a^2\langle D_{\Gamma}^2\rangle_F}{\pi^2 d\beta}. \tag{2.32}$$

Furthermore, the phonon frequencies can be evaluated using the equation (2.27), which becomes

$$\omega_{LO/K}^2 = \frac{\alpha_{\Gamma/K}}{d} ln|q| + C, \tag{2.33}$$

where $\alpha_{\Gamma/K}$ is

$$\alpha_{\Gamma/K} = \frac{2\sqrt{3}A_{\Gamma/K}a^2\langle D_{\Gamma/K}^2\rangle_F}{\pi^2\beta M} \tag{2.34}$$

and C account for all the non-divergent terms of dynamical matrix. The Kohn anomalies in SWCNT are seen in fig. 2.7. These results are derived in 0 K and the temperature

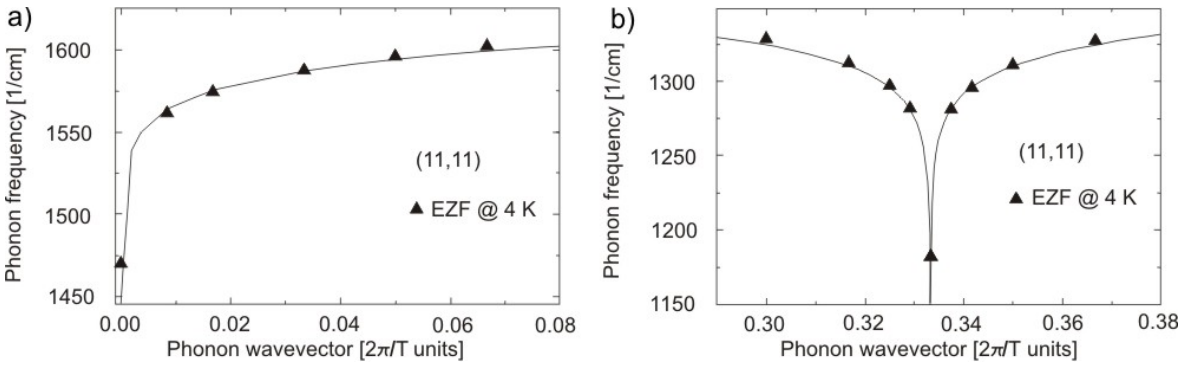

Figure 2.7: Kohn anomalies in (11,11) SWCNT at a) Γ and b) K point. Triangles are obtained from electron zone-folding density functional calculations and solid line is the plot of the equation (2.33). Adapted from the ref. [39].

dependence can also been obtained and it is [39]

$$\omega_{LO,K}^2(T) = \frac{\alpha_{\Gamma,K}}{d}\ln\frac{T}{T_0} + CC_{\Gamma,K}, \tag{2.35}$$

where T_0 is the electronic temperature in which the contributions of $\tilde{\Theta}_q$ are zero and $CC_{\Gamma,K}$ is the value of $\omega^2_{\Gamma/K}$ at $T_e = T_0$.

The phonon softening caused by KAs in metallic tubes does not depend on chirality but for LO mode in Γ and K points it is inversely proportional to tube's diameter as seen in equation (2.33). Therefore the LO modes are very different in metallic and semiconducting tubes. TO modes does not have any diameter dependence for either metallic or semiconducting tubes as expected. The following diameter dependencies can be obtained using EZF-DFT calculations [39] which are seen in figure 2.8:

$$\omega_{LO}^{M/SC} = \eta_{M/SC} + \frac{\nu_{M/SC}}{d}, \quad \omega_{TO} = \xi, \tag{2.36}$$

where $\nu_M = -77.33$ cm^{-1} nm, $\eta_M = 1597$ cm^{-1}, $\nu_{SC} = 13.78$ cm^{-1} nm, $\eta_{SC} = 1579$ cm^{-1} and $\xi = 1579$ cm^{-1}. The expression for the metallic LO phonon is completely analytical and derived from the equation (2.35) but valid only for $T_e = 315$ K. The expressions for LO semiconducting and TO modes instead are empirical but valid for any T_e.

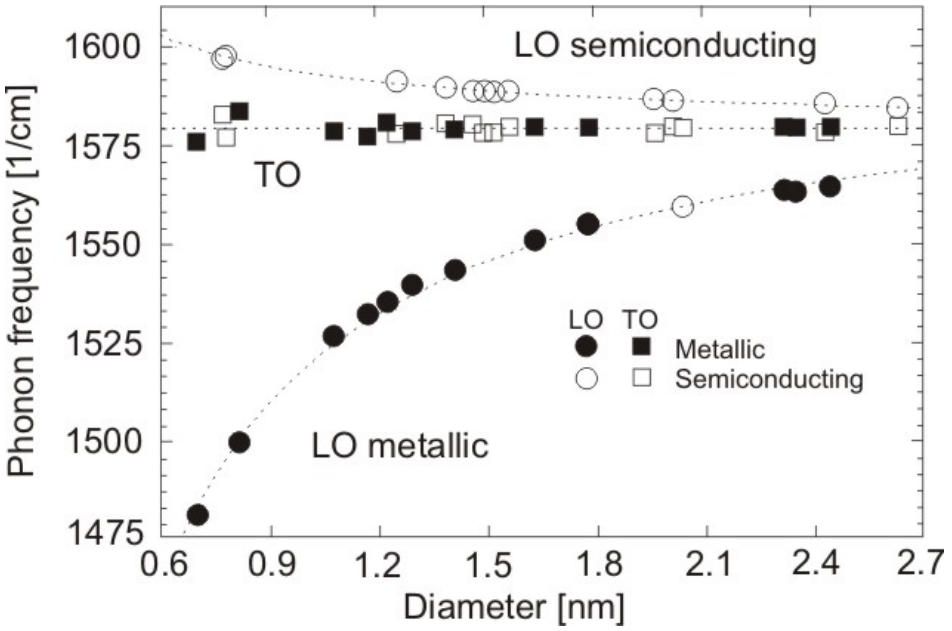

Figure 2.8: Frequency of the LO and TO modes calculated by EZF-DFT at $T_e = 315K$. Dashed lines are the fit of EZF-DFT data and correspond to he plot of equation (2.36). Adapted from the ref. [39].

In one-dimensional metallic systems, dynamic effects also have to be considered. Usually the dynamic effects are neglected in SWCNTs allthought they induce signifcant changes to the KA occurence and shape in metallic tubes. The dynamical matrix can be solved similar as for static case and the result is for LO phonon assuming that $\bar{k} >> |q \pm \frac{\hbar\omega_q}{\beta}|$

$$\tilde{\Theta}_{LO} = \frac{A_\Gamma \sqrt{3} a^2 \langle D_\Gamma^2 \rangle_F}{\pi^2 \beta d} \ln \frac{|\beta q + \bar{\omega}_{LO}||\beta q - \hbar\omega_{LO}|}{|2\beta\bar{k}|^2} \tag{2.37}$$

and for TO phonon

$$\tilde{\Theta}_{TO} = -\frac{A_\Gamma \beta q^2 \sqrt{3} a^2 \langle D_\Gamma^2 \rangle_F}{\pi^2 d[\beta^2 q^2 - (\hbar\omega_{TO})^2]}. \tag{2.38}$$

The matrix become very different compared to static case (see equations (2.31) and (2.32)). Equation (2.37) diverges when $q = \hbar\omega_q/\beta$ while in static case when $q = 0$. This tells that the KA is not at Γ. The dynamic effects are qualitatively different for LO and TO phonons and they are much bigger in TO phonons. As a conclusion it's impossible to describe the SWCNTs within static approach, which fails to describe the position of LO phonon, underestimates the TO phonon frequency and misses the Kohn anomaly at $q = \hbar\omega_q/\beta$. The differences of these approaches can be seen in fig. 2.9 [39].

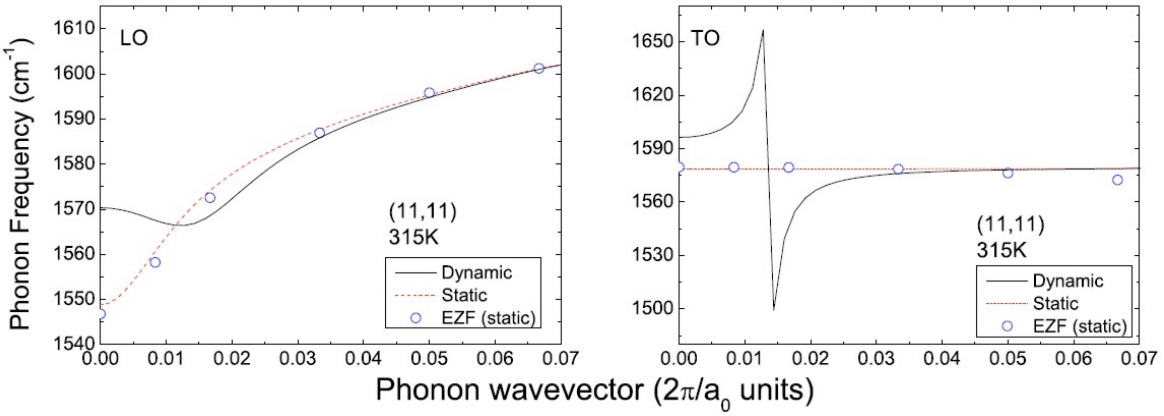

Figure 2.9: KA of the modes derived from graphene E_{2g} (close Γ) for (11,11) tube. Dots are the result of static EZF calculations, red dotted line and continuous line are obtained with analytical model based on the adiabatic (static) and non-adiabatic (dynamic) approaches. Adapted from the ref. [40].

The curvature effects are strongly dependent on tube's diameter. Also these effects split the doubly degenerate $\Gamma - E_{2g}$ phonon of graphene into TO and LO phonons in SWCNT. The graphene folding results changes in atoms separation, it loses the C-C bond planarity and mixes the σ and π states, giving as sp^2/sp^3 character to chemical bonds [39]. When combining the confinement and curvature effects the fully diameter dependence of $\Gamma - E_{2g}$ phonon modes can be obtained and that is seen in figure 2.10.

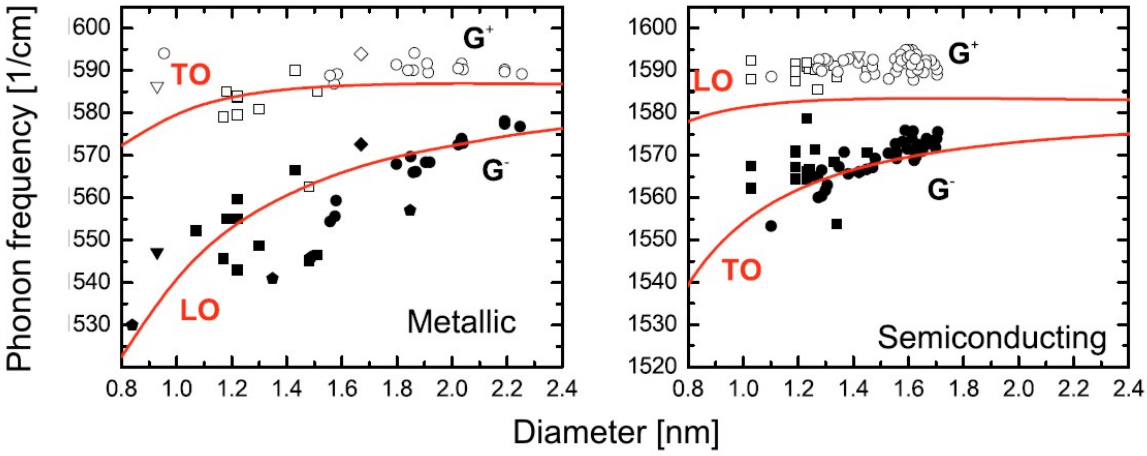

Figure 2.10: Computed frequency of the LO and TO phonons (dots) and calculated plots (red lines) that include the dynamic effects and correction for the curvature effects. Adapted from the ref. [40].

The phonon linewidths of nanotubes can be derived from EPC. The linewidth of a phonon can be divided into two terms $\gamma = \gamma^{EP} + \gamma^{an}$, where γ^{an} is due to interaction with other phonons and γ^{EP} due to interaction of electron-hole pairs [40]. The last term is therefore caused by EPC. In nanotubes γ^{an} is negligible compared to γ^{EP} so it can be used to determine the EPC in nanotubes. The linewidth of $\Gamma - E_{2g}$ phonon for LO mode in metallic tube is [40]

$$\gamma^{EP}_{\Gamma-LO} = \frac{2\sqrt{3}a_0^2\hbar^2}{\pi M\omega_\Gamma\beta}\frac{\langle D^2_\Gamma\rangle_F}{d} \tag{2.39}$$

and for TO mode

$$\gamma^{EP}_{\Gamma-TO} = 0. \tag{2.40}$$

So electron-phonon coupling results only to the linewidth of LO mode in metallic tube. For semiconducting tubes the EPC contribution is zero for both modes.

Chapter 3

Raman spectroscopy of carbon nanotubes

3.1 Introduction to Raman scattering

When electromagnetic radiation hits matter it interacts with the atoms of the matter. Most of the photons will go straight through the atom but a small part will scatter from it. If the scattering is elastic it is called Rayleigh scattering. In the case of inelastic scattering, there are two kinds of scattering processes. One is called Raman scattering and it results from the process where light is interacting with the vibrational modes of matter. That means that the photons scatter from the optical phonons. The other process is called Brillouin scattering which means that the photons are scattered from the acoustic phonons [42].

Rayleigh scattering is strong and it has the same frequency as incident radiation ν_0. That means that the molecule returns to its original energy state after excitation. But when a molecule excites between two energy states via virtual state, the process is either Brillouin or Raman scattering. From now on, we only concentrate to Raman scattering. First-order Raman scattering is three step process. The absorption of an incoming photon creates an electron-hole pair, which then scatters inelastically under the emission of a phonon, and finally recombines and emits the scattered photon. If molecule absorbs energy, the scattering is called Stokes scattering and if it loses, anti-Stokes scattering. Compared to Rayleigh scattering, Raman scattering is very weak. The scattered photon can have frequencies

$$\nu_1 = \nu_0 \pm \nu_{ph}, \tag{3.1}$$

where ν_0 is the frequency of the incident photon and ν_{ph} is the frequency of the phonon. In figure 3.1 one can see the three different scattering processes. In Raman spectroscopy, one measures the vibrational frequencies as a shift of the incident beam frequency. If the scattered beam frequency is lower than incident (minus sign), the process is called Stokes scattering and if the scattered frequency is higher, the process

is called anti-Stokes scattering [43].

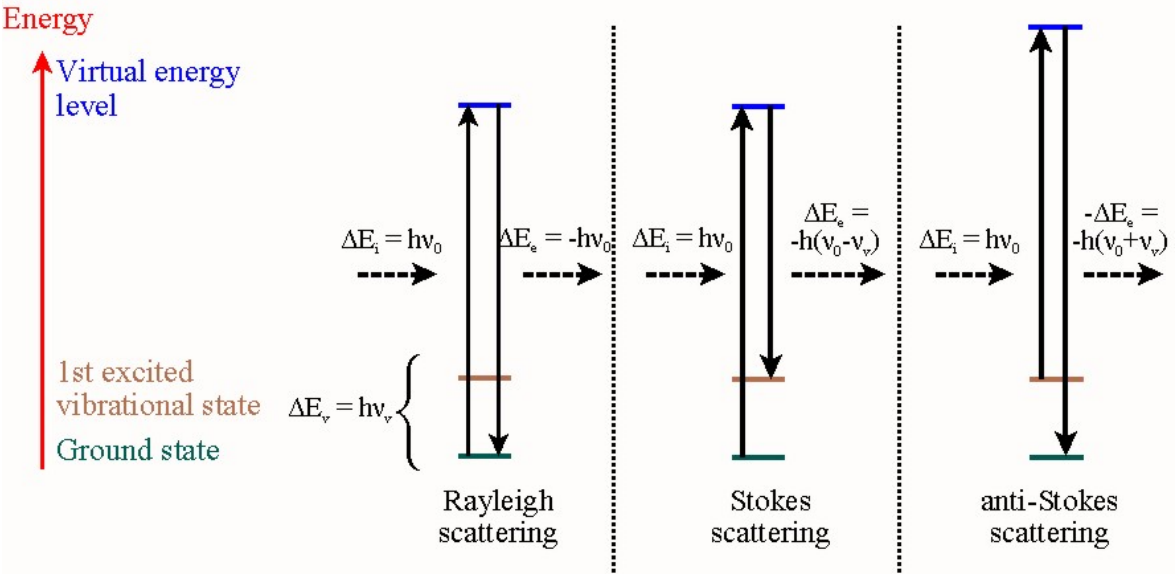

Figure 3.1: Three scattering prosesses. In the leftside there is Rayleigh scattering where molecule returns back to its ground state after emitting a photon. In the middle there is Stokes scattering where molecule excites to a vibrational (excited) state via virtual state. In the right there is anti-Stokes scattering. There molecule returns back to a lower energy state via virtual state.

We can also explain the appearence of the Stokes and anti-Stokes lines in the use of classical physics. Let's consider an electromagnetic wave $E(t) = E_0 \cos 2\pi\nu_0 t$, where E_0 is the amplitude of the wave and ν_0 the frequency of the wave. If the wave hits a diatomic molecule, an electric dipole moment P is induced

$$P = \alpha E = \alpha E_0 \cos 2\pi\nu_0 t, \tag{3.2}$$

where α is called the polarizability. If the molecule is vibrating with a frequency ν_m, the nuclear displacement q is

$$q(t) = q_0 \cos 2\pi\nu_m t, \tag{3.3}$$

where q_0 is the vibrational amplitude. In small amplitudes polarizability α depends linearly on q so we can write it as a Taylor series:

$$\alpha = \alpha_0 + \left(\frac{\partial\alpha}{\partial q}\right)_{q=0} + ... \tag{3.4}$$

Combining equations (3.2), (3.3), (3.4) we get

$$\begin{aligned} P &= \alpha E_0 \cos 2\pi\nu_0 t \\ &= \alpha_0 E_0 \cos 2\pi\nu_0 t + \left(\frac{\partial\alpha}{\partial q}\right)_{q=0} q E_0 \cos 2\pi\nu_0 t \\ &= \alpha_0 E_0 \cos 2\pi\nu_0 t + \left(\frac{\partial\alpha}{\partial q}\right)_{q=0} q_0 E_0 \cos 2\pi\nu_m t \cos 2\pi\nu_0 t. \end{aligned} \tag{3.5}$$

Using a trigonometric formula $2\cos x \cos y = \cos(x+y) + \cos(x-y)$ we get the equation (3.5) in the form

$$P = \alpha_0 E_0 \cos 2\pi\nu_0 t + \frac{1}{2}\left(\frac{\partial\alpha}{\partial q}\right)_{q=0} q_0 E_0[\cos 2\pi(\nu_0+\nu_m) + \cos 2\pi(\nu_0-\nu_m)]. \tag{3.6}$$

The first term descripes Rayleigh scattering, the second term anti-Stokes scattering and the third Stokes scattering. So if the derivative $\partial\alpha/\partial q$ is zero, the vibration is not Raman-active.

3.2 Raman spectra of SWCNTs

Carbon nanotube has 6N phonon modes for the tube whose unit cell contains 2N carbon atoms and only six of them are Raman active [44]. Raman spectra of individual SWCNT can be obtained because of the very large density of states close to van Hove singularities of this one dimensional structure. The interband excitations happen between van Hove singularities. As stated before, each tube has its own unique properties depending on its chirality and diameter as presented in table 2.1.

Resonance Raman (RR) is the case when the excitation energy of the laser is in the resonance of one of the excitations between VHSs. So the laser just picks those tubes whose excitations are in the resonance of the laser. In the case of RR, one could obtain huge enhancement in Raman cross-section (in order to $\sim 10^6$). This leads to an increased probability for Raman scattering of that excitation. With this technique one can obtain Raman spectra even on a single, isolated carbon nanotube. The polarization of the laser light has a strong importance to the intensity of the Raman peaks. The optical spectra of CNTs are dominated by the absorption/emission of light polarized parallel to the tube axis [10].

Kataura plot in fig. 3.2 plots the excitation energy as a function of tube's diameter and radial breathing mode (RBM) frequency (see sec. 3.2.1). Actually there are several different Kataura plots obtained from theoretical and experimental studies where the transition energies of the tubes are plotted either as a function of diameter or RBM frequency (see e.g. [45], [46]).

SWCNT Raman spectra is shown in fig 3.3. Three major peaks can usually be seen in the spectra: radial breathing mode (RBM), D-band and G-band. Sometimes first

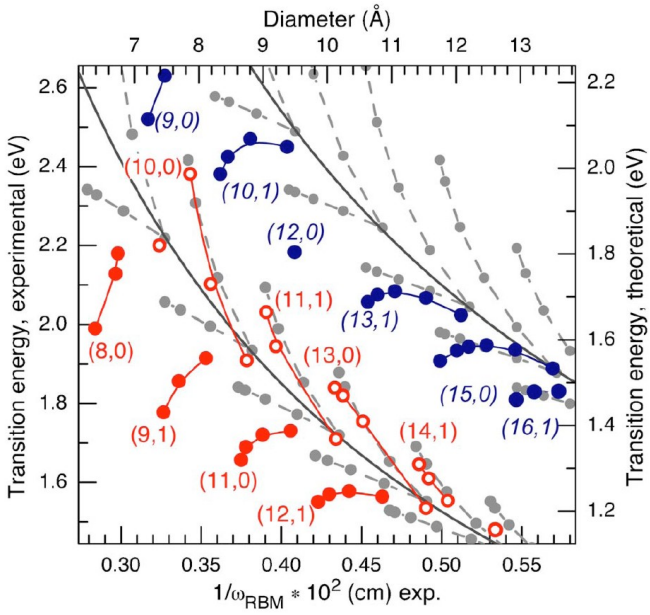

Figure 3.2: Kataura plot where second optical transitions of semiconducting nanotubes E_{22}^S (lower band) and first optical transitions of metallic nanotubes E_{11}^M (upper band) are shown. Large coloured dots are obtained from experimental data and small gray circles from theoretical data. The solid lines give the approximate 1/d dependence of the transition energies. The dashed lines indicate the V-shaped branches, where the chirality of the tube is related to its left neighbour (n, m) by $(n', m') = (n - 1, m + 2)$. The assignment in the experimental data is given for the first tube of each branch. The semiconducting tubes are divided into two families with $\nu = (n - m) \text{mod } 3 = -1$ (full circles) and with $\nu = +1$ (open circles). Adapted from the ref. [45].

harmonic of the D-band called G'-band can also be seen. RBM and D-band will be introduced briefly on following sections and the main focus is on G-band properties, which had the main contribution for this work.

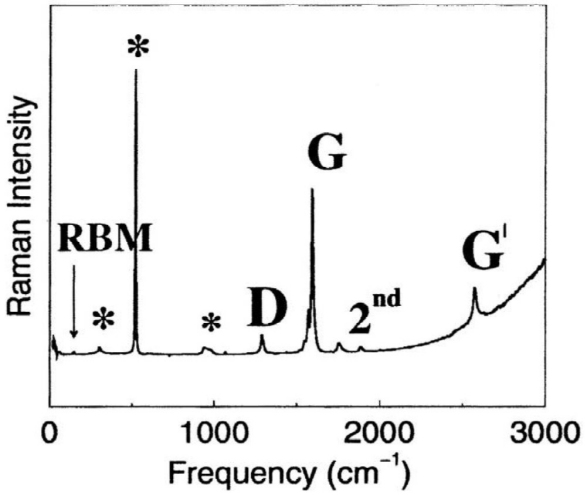

Figure 3.3: Raman spectrum of nanotube showing RBM, D-band, G-band and G'-band. * are from the Si/SiO_2 substrate. Adapted from the ref. [46].

3.2.1 Radial breathing mode

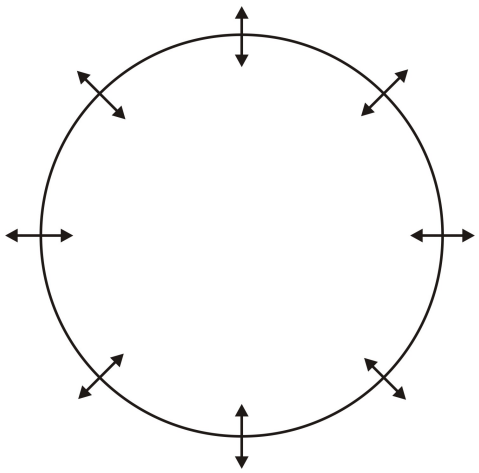

Figure 3.4: Radial breathing mode of carbon nanotube.

RBM occurs in the frequency region of 100–400 cm^{-1}. In this mode, the carbon atoms move radially and the diameter of tube varies as seen in figure 3.4. The frequency of the mode is inversely proportional to tube's diameter:

$$\omega_{RBM} = \frac{\alpha}{d_t} + B, \tag{3.7}$$

where $\alpha = 214 - 248$ cm^{-1} depending from the enviroment. For example tubes on SiO_2 substrate, measurements have given $\alpha = 215$ cm^{-1}nm and $B = 18$ cm^{-1}. When

knowing the pairs of RBM frequencies and transition energies it is possible to determine the (n,m) indices of the tube. These have been also tabulated [45].

3.2.2 D-band

The D-band is observed in the 1300–1400 cm^{-1} and it is common to all sp^2-hybridized disordered carbon materials. It comes from second-order Raman process where also the phonons which are inside the BZ become active, not only phonons that are close to Γ point. The phonons that are close K points of graphene BZ become active in nanotubes because of the defects (impurities or missing atoms), finite-size effects and molecules linked to the tube's sidewalls [10]. The frequency of this band in graphene is dispersive ($\Delta\omega_D/\Delta E_L \sim 53\ \text{cm}^{-1}$) [10] and caused by a softening of the LO phonons near K points due the Kohn anomaly as described in section 2.3.

The behaviour of the band is due to double-resonance process [47]. First an electron-hole pair is created when the incident photon is absorbed. Then the electron is scattered by a phonon (or a defect) with wavevector $\vec{q}$ and scattered back by a defect (or a phonon) with wavevector $-\vec{q}$, recombining with the hole and emitting a scattered photon.The frequency of the D-band in SWCNTs has been observed to follow the relation [48]

$$\omega_D = 1210\ \text{cm}^{-1} + 53\ \text{cm}^{-1}/\text{eV} \cdot E_L \tag{3.8}$$

and it is also reported that ω_D is inversely proportional to tubes's diameter [49].

3.2.3 G-band

G-band mode occurs in the frequency range of 1500–1605 cm^{-1}. It is derived from double degenerate Raman-allowed optical mode E_{2g} of graphene Γ-point. It is an intrinsic feature of nanotubes and it is related to vibrations that all sp^2-carbon materials have [46]. The double degenerate G-band peak of graphene is splitted into two peaks G^+ and G^- in nanotubes. The modes are polarized along the tube axis (LO) and along the tube circumference (TO) as shown in figure 3.5. The shape and position for the peaks depend strongly on the electronic properties of the tube. Raman G-band consist actually more peaks than those two main peaks (G^+ & G^-) especially in defective SWCNTs. The reason is that there are then also double-resonance Raman process present [50].

The splitting between LO and TO mode in semiconducting tubes can be explained in terms of curvature as explained in section 2.3.2. In metallic tubes there has been a strong debate on the subject and different theories have been proposed [51], [52], [53], [54], [55]. In these theories the different behaviour of the G^--band in semiconducting and metallic nanotubes is explained due to phonon-plasmon coupling in metallic nanotubes. All these theories are qualitative and fail to predict in a precise, quantitative way the observed features in Raman G-band.

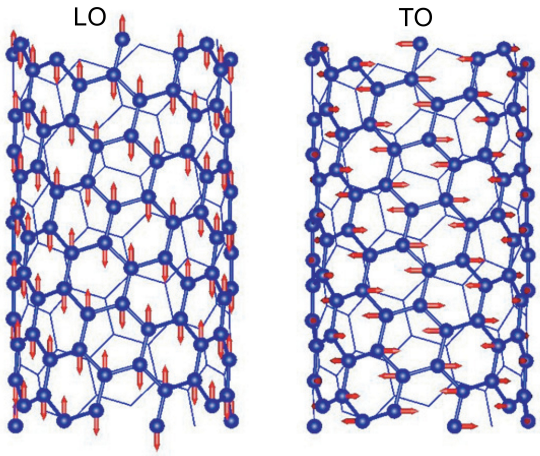

Figure 3.5: Tangential LO and TO phonon modes of SWCNT. Adapted from the ref. [40].

The newest results indicate that the splitting in metallic nanotubes is strongly induced by electron-phonon coupling and Kohn anomalies as described also in section 2.3.2. The Kohn anomaly softens only the LO mode causing that the lower frequency peak in metallic tube is the LO mode which is quite opposite than in semiconducting tube. Also it is responsible for the reduction of LO phonon lifetime, which then increases the phonon linewidth. Dynamic, time-dependent, EZF-DFT model describes therefore very well the phonon frequencies of SWCNTs and are in good agreement from data obtained from Raman spectroscopy [39]. As stated before, the frequency of higher peak ω_G^+ is not dependent on tube's diameter but the frequency of the lower peak ω_G^- depends on the diameter of the tube as follows:

$$\omega_G^- = \omega_G^+ - \frac{\xi}{d_t^2}, \tag{3.9}$$

where $\xi = 47.7$ cm^{-1} nm^2 for semiconducting tubes and $\xi = 79.5$ cm^{-1} nm^2 for metallic tubes [46].

The most striking feature that G-band has, is the well-defined difference in the lineshapes of G$^-$-peaks between metallic and semiconducting tubes as seen in figure 3.6. Therefore, it is usually used to determine whether the tube is metallic or semiconducting. For semiconducting tubes both peaks have a sharp Lorentzian shape. But for the metallic tubes, the phonon linewidth of the LO phonon (G$^-$-peak) is increased due the EPC as described in section 2.3.2. The non-zero EPC is responsible for the broad, asymmetric Breit-Wigner-Fano (BWF) lineshape which is given by [56]

$$I(\omega) = I_0 \frac{(1 + (\omega - \omega_{BWF})/q\Gamma)^2}{(1 + (\omega - \omega_{BWF})/\Gamma)^2}, \tag{3.10}$$

where I_0, ω_{BWF}, Γ and q are the maximum intensity, renormalized frequency, broadening parameter and the lineshape parameter, respectively. Because the EPC affects only

LO phonon of the metallic tube and increases the linewidth of the LO phonon, the TO phonon (G^+) remains showing a sharp Lorentzian lineshape. Therefore the lineshape of the lower frequency component between metallic and semiconducting tube is very different and it can be used to determine the metallic/semiconducting character of the tube.

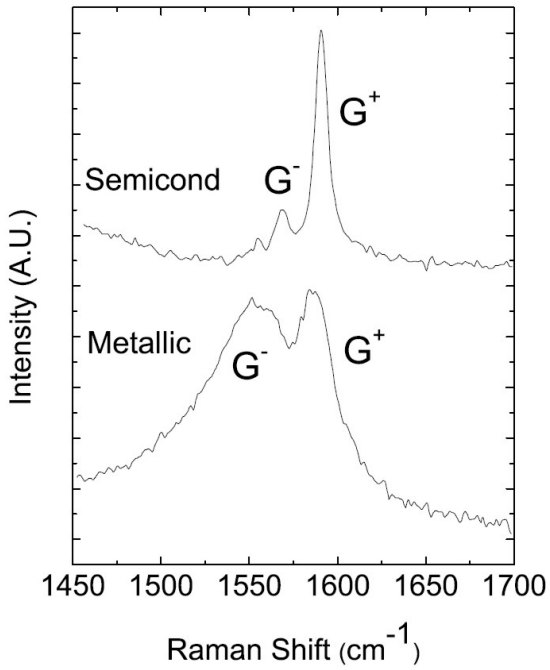

Figure 3.6: Raman G-band of semiconducting and metallic nanotubes. For semiconducting tubes there are two sharp Lorentzian peaks as for metallic the G^- peak is broad, asymmetric Breit-Wigner-Fano type of lineshape. Adapted from the ref. [40].

Chapter 4

Experimental techniques

The aim of this work was to combine the data from transport and Raman measurements and compare them in order to see if the results are consistent. So the samples had to be fabricated with such methods that they would be suitable for both measurements. Samples were chosen to fabricate in Silicon wafers with silicon dioxide layer on top of it. There was also an attempt to make transparent samples. The benefit of having a transparent sample is that one could perform also SNOM (scanning near field optical microscopy) combined with Raman spectroscopy having much higher resolution to the measurements [57]. The transparent samples were fabricated by etching a window to a Silicon chip with Silicon Nitride (Si_3N_4) layer on the both sides of the chip. The Silicon Nitride turned out to be unsuitable for the Raman measurements because of the high noise it gave to the Raman signal. Also slits were fabricated to the windows so that we could combine also TEM measurements to the tube. These samples were not used in this work because they need further development in sample fabrication but will be in the interest of study in the future.

4.1 Sample fabrication

The samples were fabricated with standard e-beam lithography on top of the highly p-doped silicon substrate with thin silicon dioxide layer on top of it. The architecture of the device is top-down so that the nanotubes were deposited first on the substrate and metal electrodes were evaporated then on the top of the tube's ends. The substrate itself was used as a backgate. This method provides lower contact resistance than depositing the tubes on top of the metal electrodes and it was chosen because it is simple to make and the contact resistance at the interface is quite small. The shematic of the fabricated devices is shown in figure 4.1. The best, and the most complicated way is to cut the tube's end and then evaporate metal into the open ends of the tube [25].

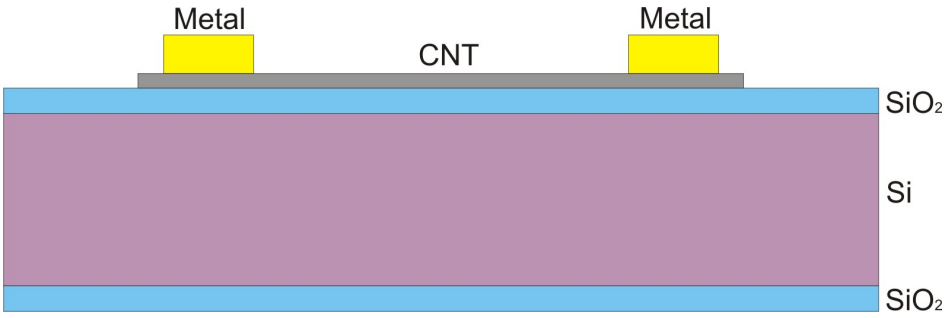

Figure 4.1: Schematic picture of the fabricated device.

4.1.1 Substrate

The chosen substrate was a highly p-doped single crystal silicon wafer. The thickness of the wafer was 500 μm and it was polished in one side. The wafer was first cut into smaller pieces which were then cleaned properly in acetone. Then the pieces were oxidized at a high temperature oven ($T = 1100°C$) in oxygen flow for 5 h in order to have thin, roughly 300 nm SiO_2 layer on top of the Si. After the oxidation the wafers were precutted from the back side with a silicon saw to 5 mm x 5 mm pieces so that each bigger piece contained 5x5 matrix of these precutted pieces.

4.1.2 Resists

Commercial Microchem positive e-beam resists were used as masks. The first layer was polymethylmethacrylate dissolved in anisole (PMMA A 3 %) with a molecular weight (MW) of 495 u and second layer PMMA A 2 % with a molecular weight of 950 u. The resists were spin coated with a spinner on the substrate with 3000 rpm for first layer and 6000 rpm for second layer. After each spinning the sample was baked on a hot plate (160 $°C$) to evaporate solvent and solidify the resist. Because the first layer had lower MW an undercut effect is formed during e-beam exposure and the lift-off of the evaporated metal becomes easier.

4.1.3 E-beam patterning

The lithography procedure contained two different patterning steps. In first step the 6x6 marker grid matrix and 28 electrodes round it were patterned for the location of the nanotubes (see fig. 4.2). Then the tubes were deposited on top of the surface and located with an AFM. Finally second exposure was done to contact the nanotubes to the outer electrodes.

The exposure of the patterns was done with Raith e-line electron beam writer and Elphy Quantum 4.0 lithography software. The exposure of the first step was done with two different working areas and aperture sizes. The inner and smaller components

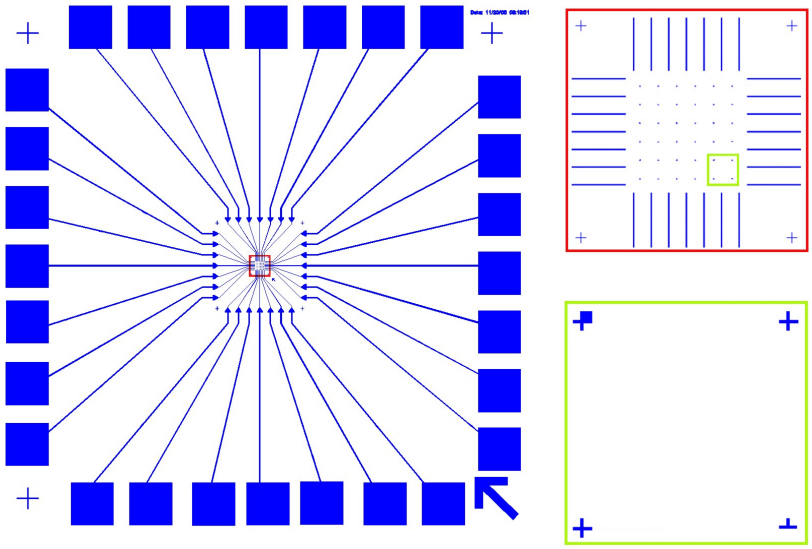

Figure 4.2: Stucture design of the first patterning where marker crosses for the second patterning, bonding pads and electrodes to the marker grid are seen. Red inset: Marker grid for locating the nanotubes. Green inset: individual markers.

were done with 500 m working area and 30 m aperture as the outer, bigger components with 2500 m working area and 120 m aperture. For both working areas the write field was the same 500 m. The exposed pattern was then developed in 1:3 of MIBK (methylisobutylketone):IPA (isopropanol) 40 s, then rinsed in IPA and dryed in nitrogen flow.

4.1.4 Metal evaporation and lift-off

The sample was cleaned in Oxford Instruments Plasmalab80Plus RIE (reactive ion etcher) for 30 s in 50 sccm oxygen flow in 40 mTorr pressure, 30 °C temperature and 60 W power. The evaporated metal was chosen to be palladium (Pd) because it makes good ohmic contacts to CNT, it has a high work function and good wetting properties for CNT [21], [28]. For the first exposure step we used a thin Ti layer (∼5 nm) to improve the adhesion before evaporating the ∼15 nm Pd layer. The evaporation was done at Balzers BAE 250T HV (high vacuum) electron beam evaporator with the evaporation speed of ∼1,3 $\AA$/s. The lift-off was done in acetone and sample was finally cleaned in IPA.

4.1.5 Nanotube deposition

The nanotubes were deposited after the first exposure step. We used commercial Nanocyl 1100-series single-walled carbon nanotubes [58], which have average diameter of 2 nm. These tubes are produced via catalytic carbon vapor deposition (ccvd) process

[59]. The SWCNT powder was dissolved in 1,2-dichloroethane and sonicated slightly before deposition on the substrate. The concentration of the tubes varied with the suspension so each deposition was made with several droplets of the tube suspension spinned with 1500 rpm on the spinner. Really long tubes (∼tens of micrometers) were also used. These tubes were grown directly on the substrate with a substrate CVD method [60]. The tubes were grown in Helsinki University of Technology at professor Esko Kauppinen's NanoMaterials group. For the long tubes the silicon substrate was undoped so it did not work at low temperatures.

4.1.6 AFM location of the tubes and second exposure

The 6x6 alignment mark matrix was then mapped with an AFM (Veeco Dimension 3100 series) using tapping mode in order to locate the tubes from the surface. The 10 μm x 10 μm images were captured so that 4 alignment marks were always seen (see figure 4.3). The captured images were transformed to the Elphy-software and aligned there to the right location. After that the contact electrodes to the tubes were easy to design.

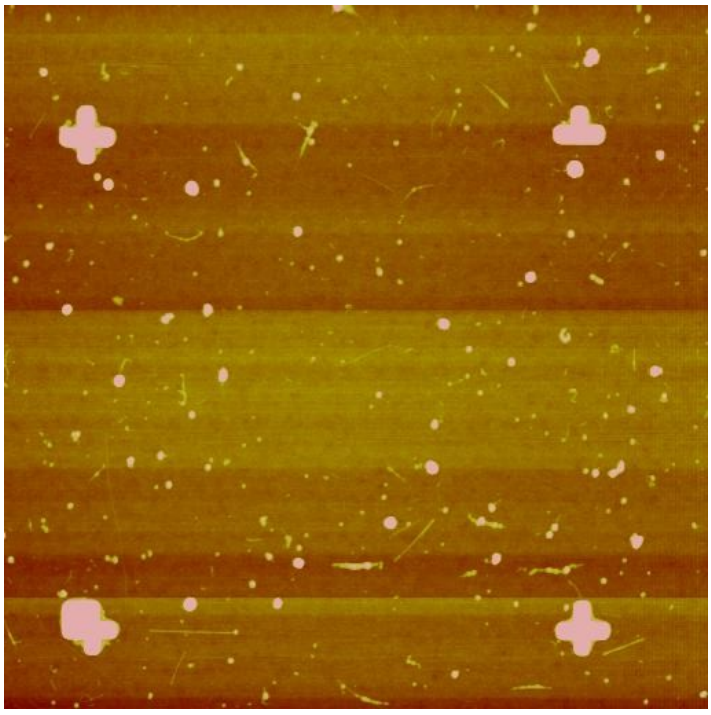

Figure 4.3: 10 μm x 10 μm AFM image with four markers and deposited nanotubes.

The second exposure step was done in order to attach the metal contacts to the tube's ends. The lithography procedure was then the same as for the first exposure step. Only the metallization was slightly different. We left the Ti adhesion layer away

so that the contacts would be from Pd. The thickness of the evaporated layer was ∼20 nm. After the second layer e-beam lithography steps the sample was checked with the AFM in order to assure that the contacts were really touching the tube (see fig. 4.4) and to measure the diameter of the tube.

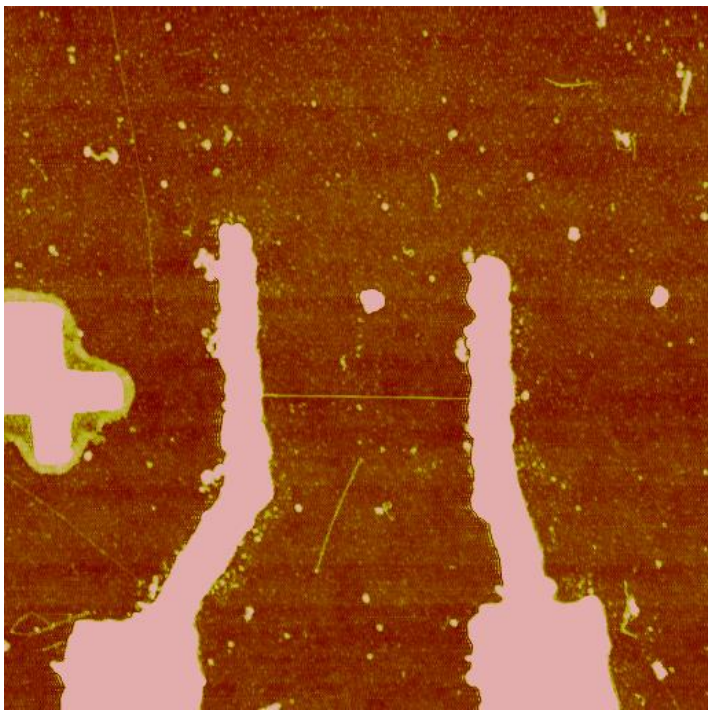

Figure 4.4: 3 μm x 3 μm AFM image from a fabricated device.

The chip was attached to the chip carrier with varnish. The chip carrier had 28 bonding pads made of gold and it could be mounted to a socket that was attached to the measurement system. The samples were connected to the chip carrier by using thin Au-wire bonded with Kulicke & Soffa 4523A thin wire bonder. Two bonding pads were used to attach the wire to the opposite edges of the chip. Those bonds were done so that the substrate could be used as a back gate. Because there were two bonds, one could obtain that the back gate truly works.

4.2 Silicon Nitride windows and slits

Also structres which had a clear optical path through the sample were fabricated. The optical path was done by etching the silicon substrate away from underneath the device. The chosen substrate was 300 μm thick, double side polished Silicon wafer which had Silicon nitride layer on top of it. The used layer thicknesses were 300 and 750 nm. The windows were done with standard photolithography and wet etching methods and the devices were fabricated on top of the windows as described in previous sections.

The etching procedure contained two different parts: removing the silicon nitride from the back side and etching the silicon away. So first thing to do was to cover the substrate with both sides in photoresist. The used resist was AZ 1514 H which was spinned on the sample at 2000 rpm and the baked on a hot plate (100 °C) for 1,5 minutes. This was done in both sides of the sample.

The desired window-structures were then exposed to the backside of the chip. The stucture we used was roughly 100 μm x 100 μm square windows. The exposure was done using UV-light with Karl Suss MA45 mask aligner. In order to have the desired stuctures, a physical mask is needed. The mask was done in a glass plate with standard e-beam lithography. After the exposure the sample was developed in 1:5 of AZ 531B (based on NaOH):distilled water for 30 s and rinsed in distilled water.

The nitride was etched away in Oxford Instruments Plasmalab80Plus RIE (reactive ion etcher). The parameters for the etching recipe were: temperature 30 °C, pressure 55 mTorr, power 150 W and the gas flow was 50 sccm for Trifluoromethane (CHF_3) and 5 sccm for O_2. After that the resist was washed away in acetone and the chips were ready for the wet etching step.

The wet etching was done in 35 % KOH (potassium hydroxide) at 97 °C temperature for 3 hours. After that the chips were carefully washed in hot purified water. The etching rate for 100 Si is reported to be ∼180 μm/h and it won't basically etch the SI_3N_4 at all [61]. The etching process is anisotropic and the etching angle is 54,7°. In order to have a window in a right size the openings done in nitride in the backside of the chip has to be larger. The relation is

$$L = \frac{2d}{\tan 54.7} + l, \tag{4.1}$$

where L is the length of the square side in backside, d the thickness of the silicon and l the length of the square (window) side in topside. For example in order to have 100 μm x 100 μm window, one has to do 525 μm x 525 μm openings to the backside. The shematic of the fabricated structure is seen on fig.4.5(a).

Structures where there was a narrow slit on the window were also fabricated. Thus the optical path will be more undisturbed which is good for optical and TEM (trasmission electron microscope) measurements. The slits were basically done on the windows just by etching the nitride away with the same treatment as described above. So just different mask is needed in order to have narrow slits. We used a mask where there

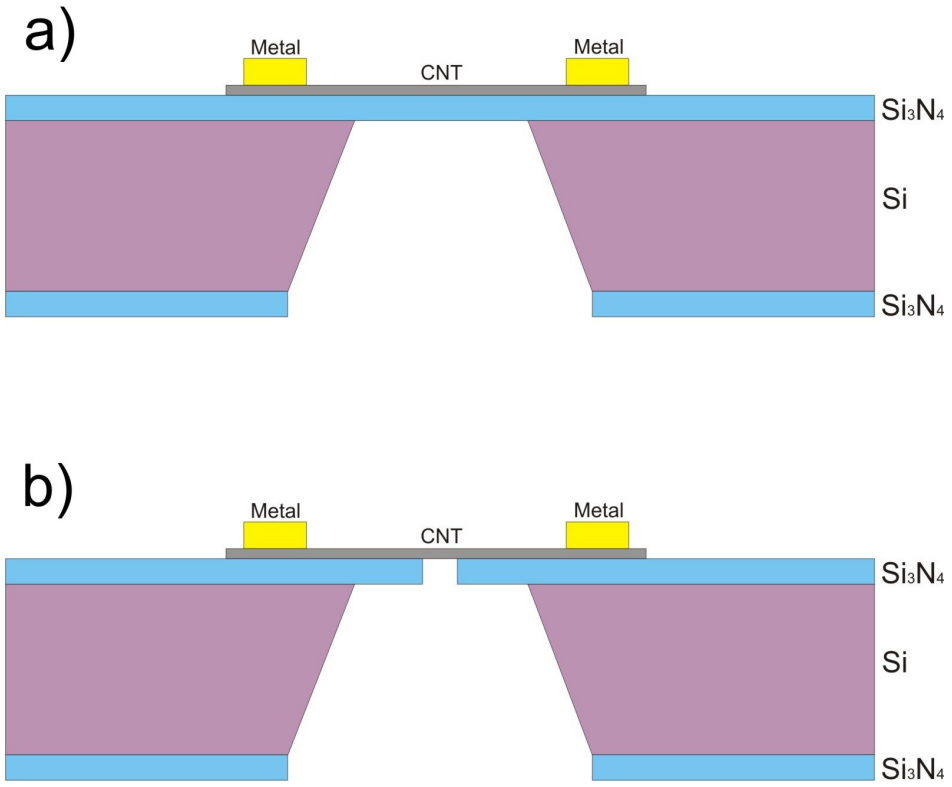

Figure 4.5: Fabricated Si_3N_4 window structure (a) and slit on the windows (b).

was 5 μm wide and 80 μm long slit. The schematic of the stucture can be seen on figure 4.5 (b).

4.3 Measurement setup

4.3.1 Transport measurements

The chip carrier was attached to a home made dipstick. The dipstick was designed and fabricated here at the Nanoscience center. It could be mounted to a liquid helium dewar at it height in the dewar could be controlled with a adjustable flange. Just adjusting the height of the dipstick one could cover the whole temperature range from room temperature to liquid Helium temperature (4.2 K). The dipstick has in total 28 measurement channels and a silicon diode temperature sensor DT-470 by Lake Shore Cryotronics. That sensor was calibrated to cover the whole temperature range.

There was a vacuum can in the end of the dipstick. The carrier was mounted to the socket, then the can was sealed with Indium ring and tightened with clamps. Finally the air was pumped away with a rough pump in order remove moisture from the can. It is important to get rid of the moisture because it condences to the surfaces when

cooling down and this can induce errors to the measurements. After pumping roughly to 0.2 bar, exchange gas (He) was led to the can to improve the heat exchange between the sample and dewar.

The measurements were simple two terminal measurements. Two terminal measurements were chosen because four terminal measurements do not work in small 1D samples because it divides the object into segments and changes the properties of the system. Also the results coincide when reaching the ballistic limit of the tube and it does not matter whether the measurements are two terminal or four terminal [20], [62].

A source-drain voltage was fed to the electrode and the current flowing through the tube was measured. The source-drain voltage and gate voltage was supplied from National Instruments (NI) BNC 2110 PXI-controlled analog I/O-connector, which was controlled by NI PXI 6281 M Series data acquisition (DAQ) device. The resolution of the DAQ was 18 bit which the limits the step size of the voltage. The signal was fed through Stanford Research Systems SR570 Low Noise Current Preamplifier. The amplifier was used as a transimpedance amplifier to convert the small current signal to easily measurable voltage and the sensitivity of the preamplifier was adjusted to 10^{-6} V/A. Then the output voltage was fed through the connector back to the DAQ device. The output voltage range for the device was -10 V...10 V. The circuit diagram is seen on figure 4.6 The resistances caused by wires are order of tens Ohms even at

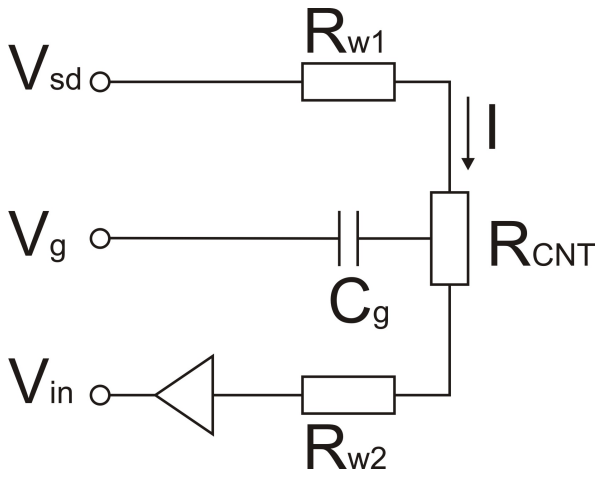

Figure 4.6: Simplified circuit diagram of measurement setup.

low temperatures. The resistance of the tube on the other hand is at its best 12,5 kΩ so the wire resistances are negligible compared to that.

4.3.2 Raman measurements

The Raman mesurements were carried out by Jyri Rintala from Mika Petterson's group at department of Chemistry. The Raman measurements were done with homemade

Raman spectrometer in a back-scattering geometry. The chip carrier was mounted to the socket which was placed to XYZ-stage in a vertical postition. The stage consist of a manual stage (Newport ULTRAling 462-XYZ-M) for coarse positioning and a XYZ-piezoscanner (Attocube ANPxyz101) for fine positioning attached on the manual stage. The piezoscanner was open-loop system having at minimum 50 nm steps in each direction. The spectral resolution for this setup was measured to be 3-4 cm^{-1} with 600 g/mm grating.

Two different laser sources were used: Alphalas Monolas-532-100-SM with 532 nm excitation wavelength and Melles Griot 25-LHP-991-230 with 632.8 nm excitation wavelength. The excitation light was focused to a sample with a microscope objective (Olympos 100x, 0.70 N.A.) and the backscattered light was collected with the same objective. Also a beam splitter, an extra lens and a 10x microscope ocular was used in order to have an optical microscope with 1000x magnification. The optical microscope is needed to position the laser spot in the desired area of the sample. The Rayleigh scattering was filtered away with a Semrock edge filter that allows to record the Raman spectrum down to 70 cm^{-1}. Then the scattered light was dispersed in a 0.5 m imaging spectrograph (Acton SpectraPro 2555i) using 600 g/mm grating and finally detected with an EMCCD camera (Andor Newton EM DU971N-BV) using a 60 μm slit width. The shematic drawing of the measurement setup is seen in figure 4.7.

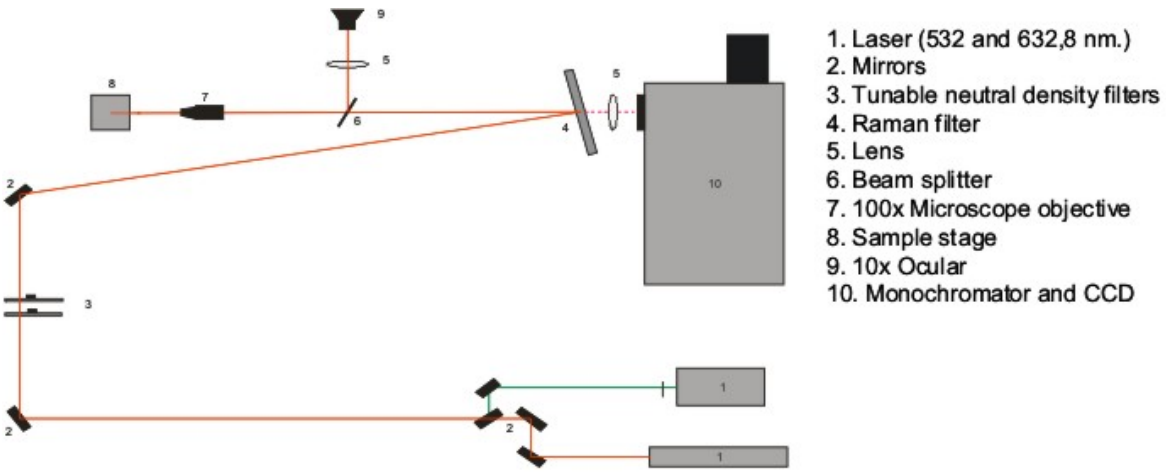

Figure 4.7: Raman measurement setup.

In order to have a good signal to noise ratio, the signal was accumulated from 200 measurements with 2 s data collecting for each measurement.

Chapter 5

Measurements and results

Both transport and Raman mesurements were carried out from the samples. In total there were 5 samples in which both of the measurements were performed. Four of them were made from the Nanocyl tubes with the channel lengths of 380 nm to 890 nm. The fifth tube instead on the other hand was made with substrate CVD method and had the channel length of 20 μm.

5.1 Transport measurements

The transport measurements were performed in a vacuum at various temperatures between room temperature and liquid Helium temperature (4.2 K). The total of 5 different devices were measured. The resistance of the tubes at room temperature varied from $\sim$ 100 kΩ to $\sim$ 10 MΩ when measured with zero gate voltage. Since the minimum resistance of a ballistic tube is 6.5 kΩ there is a remarkable contact resistance at the interfaces and Schottky barrier model (see section 2.2.1) can be used to describe the device (see e.g. [23]).

5.1.1 Gate dependency of semiconducting nanotube

Semiconducting material should be sensitive to a gate voltage as metallic device should not respond that at all. The same is also valid for carbon nanotubes. In this section we concentrate solely on semiconducting nanotubes and gate modulation based on the Schottky barrier model described in section 2.2.1. The gate voltage shifts the bands of the nanotube and therefore changes the thickness of the Schottky barrier at the interface. The tunneling current depends exponentially from the gate field. Increasing positive voltage cause bands to shift downwards and increasing negative voltage upwards. So in the case of high work function metal and relatively small band gap CNT (ie. $\phi_M < E_g/2 + \phi_{CNT}$) at zero gate voltage, the metal Fermi level and charge neutrality level of nanotube meet each other which causes the bands to bend downwards at the interface (see fig. 5.1 (a)). A small tunneling current flows through

the Schottky barrier to the valence band of the nanotube. Increasing the negative gate voltage shiftes the bands upwards reducing the barrier thickness. This causes the current increases through the barrier. At some voltage value the valence band is approximately at the same level than metal Fermi level. The value of that voltage is called threshold voltage V_{TH} (fig. 5.1 (b)) and the charge starts to accumulate in the tube. After that the device is sensitive to changes in gate voltage and the current grows rapidly. After some point the current starts to saturate and further increasing of the voltage does not affect the current so much anymore. (5.1 (c)). The reason is that voltage does not affect the band shifting as much and the barrier thickness remains roughly at the same value. The current is now on its maximum value (ON-state) and one can obtain the minimum resistance (ie. contact resistance) of the device. When increasing the gate voltage to the positive direction the bands start to shift downwards. At certain voltage the charge neutrality level aligns with the metal Fermi level and the bands are flat. In that case the only current that flows is due the thermal energy and the device is on its OFF-state (fig. 5.1 (d)). Increasing more voltage the tunneling to the conduction band of tube starts to play a more significant role (fig. 5.1 (e)). Thus the behaviour of this particular device can be changed from p-type to n-type character although the current through the device is smaller because the barrier thickness is wider when the boundary condition described above is satisfied.

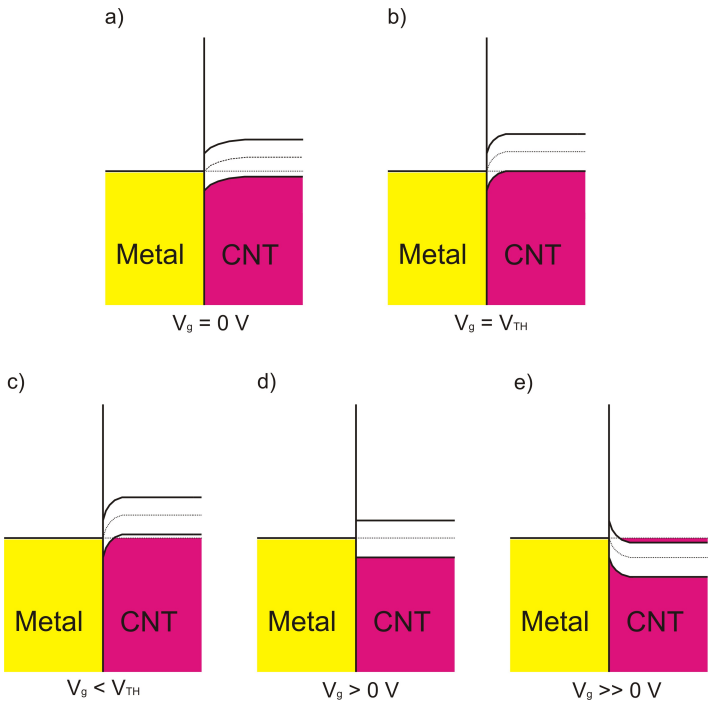

Figure 5.1: Gate modulation of the Schottky barrier with an inteface dipole present.

5.1.2 Gate measurements

The measurements were done in low bias regime i.e. $V_{DS} = 10$ mV for all tubes. We will first discuss the measurements done in nanocyl tubes because of the similar device geometry and then in the end the one tube with relatively long channel length. Two devices showed clear gate dependency already at room temparature. It means that there is a remarkable gap in the nanotube. Usually the tube is manifested to be semiconducting when the ON/OFF ratio of the tube is at least a decade and these tubes had the ratio of $\sim 10^2$. Both tubes also showed clear ambipolar behaviour having stronger p-type response as it should be in our case. The ON-current in p-type side was roughly $\sim 10^1$ times larger than n-side. When lowering down the temperature the ON/OFF ratio and non-conducting gap are between p-type and n-type behaviour started to increase. The largest ON/OFF ratios in order of $\sim 10^4$ were observed at ~ 75 K and then the ratio started to decrease a little bit when cooling towards liquid Helium (lHe) temperature (4.2 K). Two of the devices did not show clear dependency from the gate voltages and the ON/OFF ratio was only $< \sim 2$. These tubes can be either small band gap semiconducting tubes or metallic tubes. If the tubes were small band gap semiconductors then the thermal energy would be sufficient to excite the charge carriers from metal Fermi level to the valence or conduction band of the tube. This means that the band gap should arise when cooling down the temperature. The ON/OFF ratio of these two samples increased a little bit when cooling down but it is impossible to say from these measurements whether the tube is truly metallic or not. The gate dependency for tube with semiconducting behaviour is seen on figure 5.2 and for tube with metallic behaviour in figure 5.3.

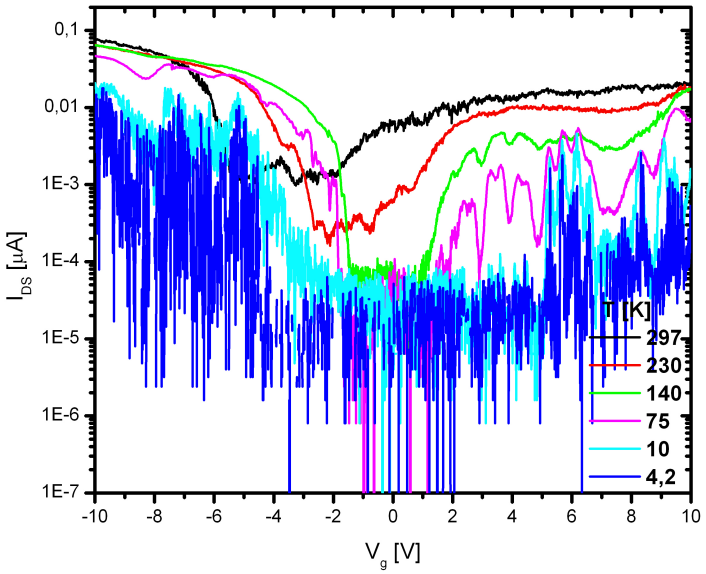

Figure 5.2: Gate dependency of the tube with semiconducting behaviour at different temperatures.

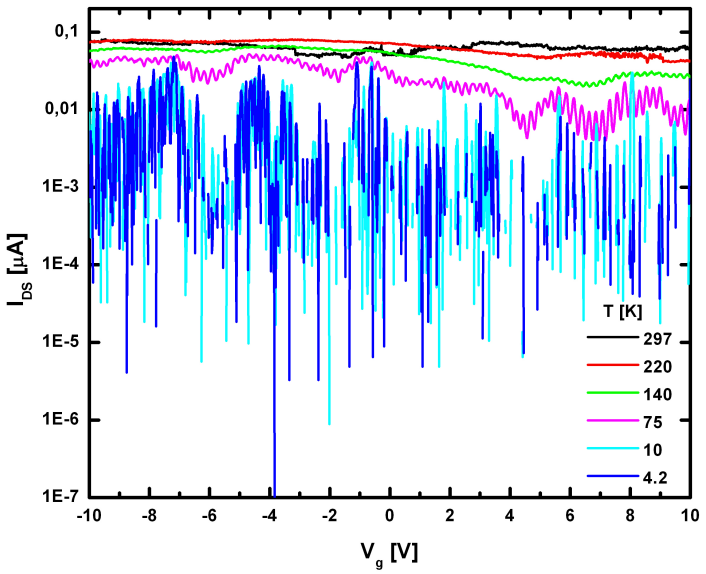

Figure 5.3: Gate dependency of the tube with metallic behaviour at different temperatures.

A clear hysteresis was also present at the gate curves depending from the gate voltage sweep direction when measuring at room temperature. This is seen on figure 5.4. The threshold voltage of the device is shifted and the difference is as much as 10 volts. The hysteresis loop was diminished by lowering the temperature and the gap was vanished completely in $\sim$ 130 K. Several theories of the origin of the hysteresis in CNTs have been proposed [12]. One suggests that the dielectric layer can relocate in response to the applied gate voltage which then modifies the local electric field sensed by the charge carriers in the tube. Second theory proposes that there are stationary charge traps in the dielectric in the vicinity of the tube. These traps could then be filled or emptied with the charge carriers of the CNT. Charge carriers then screen the gate voltage which causes the hysteresis. Third theory suggests that defects in the nanotube itself could act as charging centers which can be filled or emptied with the gate field. Also surface chemistry has proposed to play a role in the hysteresis. Recent studies suggest that the main contribution to the hysteresis comes from stationary charge traps in the dielectric material [12]. The hysteresis is an unwanted feature when utilizing carbon nanotube field-effect transistors but can be exploited as memory elements [12], [10].

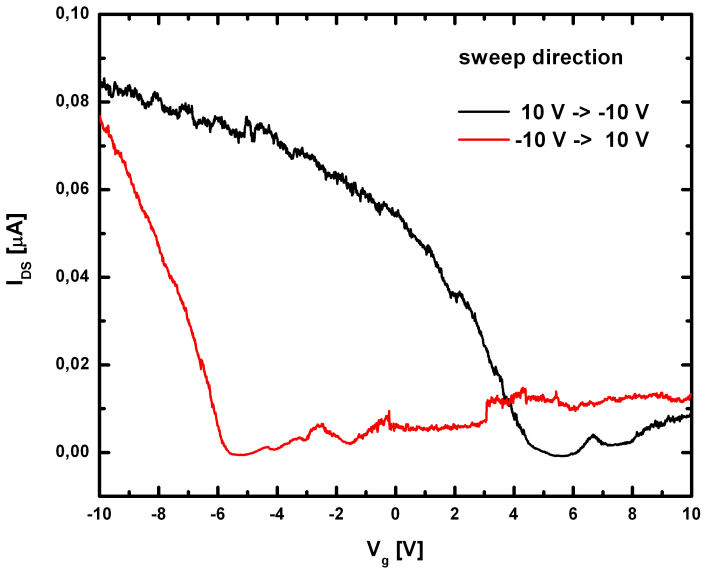

Figure 5.4: Hysteresis loop of semiconducting SWCNT at room temperature.

5.1.3 Coulomb blockade

In figure 5.3 a clear oscillations is seen as a function of gate voltage. The oscillations become visible when the temperature is lowered to 75 K or below. These oscillations are clear evidence of Coulomb blockade in the sample [63]. In the Coulomb blockade (CB) model the period between two peaks is

$$\Delta V_g = \frac{C}{eC_g}(\Delta E + \frac{e^2}{C}), \tag{5.1}$$

where C is the total capacitance of the tube, C_g the capacitance between backgate and tube and ΔE the single particle level spacing. The ratio of $C_g/C =: \alpha$ is defined as the gate efficiency factor [64]. Also the peak width is a function of temperature and is given by [64]

$$\frac{d(\Delta V_g)}{dT} = \frac{3,5k_B}{e\alpha}. \tag{5.2}$$

In figure 5.5 the temperature dependence of the peak is seen. From that data the peak width as a function of temperature can be deduced. Taking the linear fit of the data one gets that peak width $W = 7,97 \cdot 10^{-4}$ V/K. Putting that value to the equation (5.2) one gets the gate efficiency factor $\alpha = 0,38$. This is consitent with the report from the other group [65]. The gate capacitance between a wire above infinite plate is

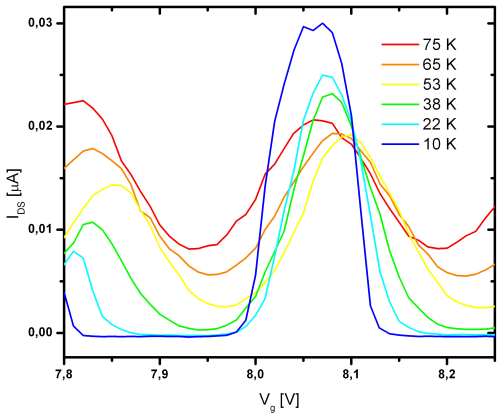

Figure 5.5: Coulomb blockade oscillation peaks at different temperatures.

given by

$$C_g = \frac{2\pi\epsilon_r\epsilon_0}{\ln\frac{2h}{r}}, \tag{5.3}$$

where ϵ_r is the relative permittivity of the dielectric, h the thickness of the dielectric layer and r the radius of the tube. In our case, dielectric for thermally grown SiO_2 is

$\epsilon_r \approx 3,9$, thickness roughly 300 nm and the radius of the tube 0,4 nm. With these values we get the gate capacitance of $C_g \approx 2,967 \cdot 10^{-11}$ F. Furthermore, we can estimate the total capacitance of the system $C = C_g/\alpha \approx 7,807 \cdot 10^{-11}$ F. The total capacitance per unit length is then (channel length is 380 nm in this particular tube) $c = 2,055 \cdot 10^{-4}$ F/m. Finally we obtain the level spacing of the tube from equation (5.1). The period of the peaks is 240 mV so the level spacing is then $\Delta E = e\alpha\Delta V_g - e^2/C \approx 91$ meV. Either the tube is a small band gap semiconductor or then only a fraction of ∼10 nm of the tube is acting as a quantum dot.

5.1.4 I-V measurements

The I-V curves at room temperature were linear in all cases. The bias range was -0,1 V...0,1 V which can be too small in order to see any nonlinearity. At lower temperatures also the bias range was increased to -0,3 V...0,3 V which was still slightly too small especially for semiconducting tubes. The semiconducting behaviour appeared more pronounced when cooling down. In the figure 5.6 there is I-V curves of the semiconducting tube at lHe temperature with different gate voltages. It is clearly seen that there is a plateau in the curve even on its ON-state. This is a clear evidence of tunnel barriers (Coulomb blockades) in the system. Most likely the barriers are in the contacts (i.e. Schottky barriers) in which the relative high contact resistances also amplify. The plateu then broadens when increasing the gate voltage to the gap region and then starts to decrease again when going to n-type region. The nonlinearity also started to form for tubes with metallic behaviour when reducing temperature. An I-V curve of metallic-like tube at different temperatures is shown in figure 5.7. The plateau then also suggests that there are Coulomb blockades, which were also seen from gate curve. Other option is that there is a small band gap present in the tubes which becomes to see when the thermal energy is reduced enough. The ON-state resistances at lHe temperature for the semiconducting tubes were in the region of $\sim 120\ k\Omega - \sim 250\ k\Omega$ and the resistance for the metallic tubes $\sim 120\ k\Omega - \sim 330\ k\Omega$.

Both semiconducting tubes showed negative differential resistance (NDR). The NDR can occur for example for metallic nanotubes in high bias regime due to the self-heating effect [66]. Another example is that the tube is acting as resonant tunneling diode [67], [68]. In our samples the NDR was visible in 4,2 K at certain positive gate voltages. The region, where the effect arises was at the negative edge of the plateu in I-V curve. The NDR is seen on figure 5.8. In our case, the origin of the effect is probably because the device is acting as a resonant tunneling device (quantum dot). This can happen at certain gate voltage in the OFF-state of semiconducting device. The current is mainly driven by tunneling through the localized states of the quantum dot. When the localized levels of the quantum dot are in resonance with the Fermi-levels of the system the current increases, and starts to decrease when the system is driven over the broadened localized level of the quantum dot [68].

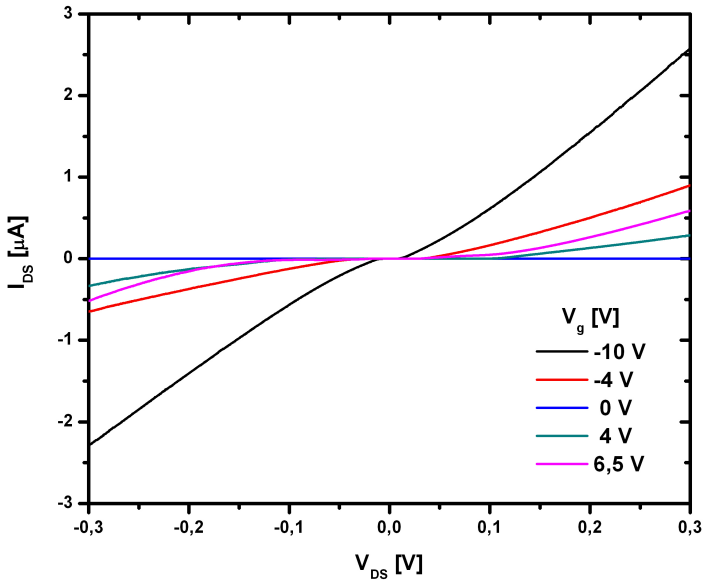

Figure 5.6: I-V curve of semiconducting tube at 4,2 K with different values of gate voltage.

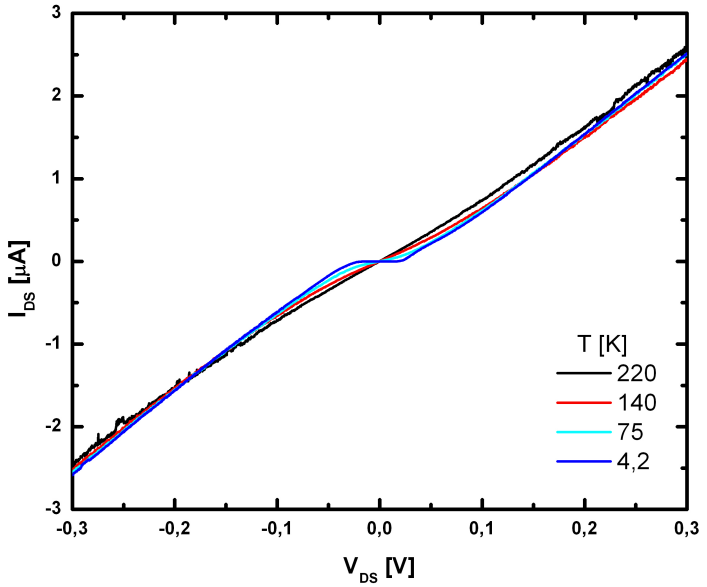

Figure 5.7: I-V curve of metallic tube at different temperatures at $V_g = 0$ V.

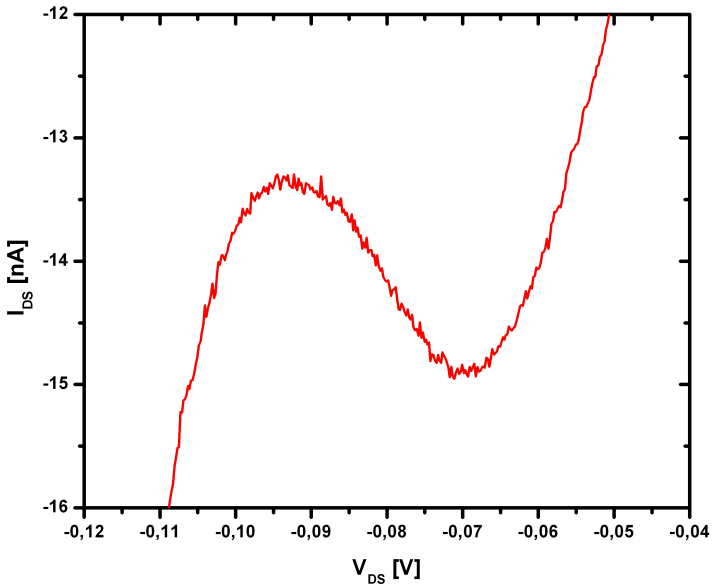

Figure 5.8: Negative differential resistance in semiconducting nanotube at 4,2 K. Gate voltage is 6,5 V.

We also did measurements to one long tube (channel length 20 μm) fabricated with substrate CVD method at HUT. The tube showed semiconducting behaviour and the results were quite similar to the two shorter Nanocyl tubes. The resistance of the tube at room temperature and zero back gate voltage was $\sim 5M\Omega$ and the ON/OFF ratio of the tube $\sim 10^1$. The back gate did not work at the lowest temperatures because the silicon substrate was not doped so the measurements concentrated only on the temperatures above liquid Nitrogen temperature.

5.2 Raman measurements

The Raman G-band was used to determine whether the tube is semiconducting or metallic. The RBM mode gave additional information about the tube's structure and gives a way to determine the indices of the tube. Semiconducting and metallic behavior of the tube can be seen very clearly from the G-band peaks as described in section 3.2.3.

In the use of Kataura plot it is possible to assign the chiral indices of the tube when the laser excitation energy and RBM mode frequency are known [45]. The first step is to obtain the ω_{RBM} at given excitation laser energy E_l. Then the excitation energy has to be put into the Kataura plot (see for example fig. 3.2). The tube which is closest to the excitation energy at given ω_{RBM} is most likely the tube that has been measured. This method provides a good way to assign the indices of relatively small tubes. It relies on the first transition for metallic tubes and second transition for semiconducting tubes. Especially in the case of semiconducting tubes having $d > 1,3$ nm, E_{22}^S is already in the infrared range [69]. It means that indices cannot be determined with this method for large diameter semiconducting SWCNTs. The third and fourth optical transitions, however, can be used to determine the indices in that case and an experimental data about these transitions for semiconducting tubes are presented in reference [69].

The Raman measurements confirmed the observations done in transport measurements. Both semiconducting-like Nanocyl tubes showed also clear semiconducting behaviour in Raman G-band. Both tubes also had a visible D-band and strong RBM. What is remarkable for the other semiconducting tube is that the G^--band is stronger than G^+-band. The reason for that is still unclear and needs further investigation. A Raman spectra of a semiconducting tube is shown on figure 5.9. A clear double peak structure in G-band is seen and the peak positions are 1559.8 cm^{-1} and 1587.3 cm^{-1}. Both peaks have sharp Lorentzian shapes as it should be for semiconducting nanotube. The intensity of the peaks is quite opposite than one could expect as said above. The RBM lies at 103.5 cm^{-1}. The diameter of the tube can be obtained from equation (3.7) and it is for this particular tube 2,48 nm. The measurements done with AFM gave a diameter of ∼2,7 nm which is consistent with the data obtained from the RBM mode. Furthermore it is possible to try to do an assignmation of the indices by the use of higher optical transitions [69] combined with the RBM-mode results. The possible chiralities obtained with this method for the tube presented in fig. 5.9 are (22,14), (26,9), (25,11) or (31,2).

Two tubes that showed metallic behaviour in transport measurements were also confirmed to be metallic in Raman measurements. Both tubes had relatively strong D modes and RBM modes. The Raman spectra of metallic tube is presented in figure 5.10. A clear double peak sturcture is seen on G-band. The lower peak having a maxima at 1537.9 cm^{-1} is very broad and the higher peak having a maxima at 1589.2 cm^{-1} is sharp Lorentzian-shaped as it is expected to be in metallic nanotube. The D mode is clearly visible and its center lies at 1321.6 cm^{-1}. The RBM is very sharp

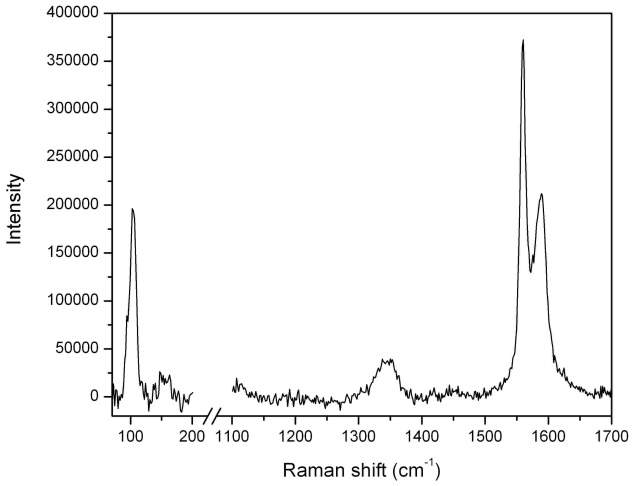

Figure 5.9: The Raman spectra of semiconducting tube.

and it lies at 220 cm^{-1}. The diameter calculated from RBM position by using the equation (3.7) is 1.08 nm which is also consistent with the AFM data (diameter 0,8 nm). This tube is assigned to the chiral indices of (12,3). The assignmation is done by the procedure explained earlier in this section.

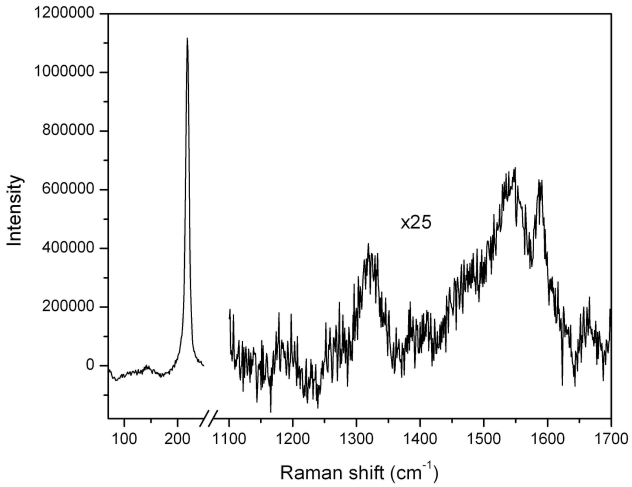

Figure 5.10: The Raman spectrum of metallic tube.

Raman measurements done for the long tube showed clearly that the tube was semiconducting as also transport measurements did. The RBM-mode was not visible

for the tube, so neither diameter nor chiral index assignment could be done. Measurements along the tube axis on the other hand could be done. They showed that the tube had an uniform structure along the tube axis.

Chapter 6

Conclusions

The properties of SWCNTs were studied by doing both electrical transport measurements and Raman measurements for the tube. We fabricated devices made of tubes from two different kinds of nanotube sources on top of two different kinds of substrates. The other substrate having a Si_3N_4 window in the substrate was made in order to do high resolution SNOM measurements from the tube. The problem of the material was that it caused too much noise to the Raman measurements and it had to be abandoned. Another more promising way was to etch an opening to the window or use thin and flat glass chips as a substrate. These methods need more study but could provide a promising way to study CNTs in greater detail.

The actual samples which were measured were fabricated on top of the Si/SiO_2 substrate and detailed transport and Raman measurements were performed to 5 different devices. The transport measurements were done in the temperature range varying from room temperature to cryogenic temperatures. The measurements distinguished metallic and semiconducting tubes very clearly. Both I-V and gate measurements indicated the tube type to be either metallic or semiconducting. The relatively high contact resistances indicated that there were remarkable Schottky barriers at the interfaces. Therefore the semiconducting behaviour of the devices was explained i the use of the Schottky barrier model. The ON/OFF ratios of semiconducting tubes in room temperature were roughly $\sim 10^2$. Also a clear hysteresis was observed in gate curves at room temperature which diminished when lowering the temperature. The low temperature measurements also showed NDR in two semiconducting devices at the OFF-state. This effect most likely origins from the fact that the device is acting as a resonant tunneling device. It would need much more measurements and theoretical calculations to fully understand this behaviour. Some estimations of the band gap could also be done for semiconducting tubes. To get more accurate results, it would need more detailed measurements in low temperatures. Especially the bias range was way too small for the relatively large semiconducting nanotubes we measured. One of the metallic tubes showed clear Coulomb blockade oscillations at relatively high temperatures. From that data it was possible to determine the electrostatic lever arm of

the tube. That lever arm could be used to determine if the tube was really a small band gap semiconducting tube. It is however almost impossible to distinguish if there is a small band gap or just Coulomb blockades with these measurements and it would need more measurements to verify that.

The Raman measurements were done using either a 632.8 nm or a 532 nm laser as the excitation source. The different lineshapes of Raman G-band was used to determine whether the tube is metallic or semiconducting. The G-band lineshapes distinguished metallic and semiconducting tubes very clearly. One semiconducting tube had a strange feature of having more intense G^- peak than G^+ peak. This is usually not the case and it will still need more investigations in order to explain the origin of it. From the RBM mode, the diameter of the tubes were obtained and furthermore, in the use of RBM data together with experimental Kataura plots, an assignment to the tubes were performed. Metallic tubes were assigned using first optical transitions and semiconducting tubes using third and fourth optical transitions. All of the tubes had relatively strong D-band which could indicate that the tubes have defects in their structures.

Table 6.1: Measured nanotubes and their properties

Tube	**Type**	**d (RBM) [nm]**	**d (AFM) [nm]**	**Channel length [μm]**	**(n,m)**
A	M	1,08	0,8	0,38	(12,3)
B	M	1,22	1,6	0,75	(13,4)
C	SC	1,85	2,6	0,85	*
D	SC	2,48	2,7	0,89	**
E	SC	-	2,7	20	-

* possible indices are (22,3), (17,10), (23,1), (16,11)

** possible indicec are (22,14), (26,9), (25,11), (31,2)

The electronic transport and Raman measurements were consistent with each others and both methods gave the same results of the type of the nanotube. Two tubes showed clear metallic behaviour and three tubes semiconducting behaviour. The assignment done to the metallic tube (tube A) that was having clear Coulomb blockade oscillations suggests that the tube really would have a small band gap. The other metallic tube was manifested to be either (9,9) truly metallic tube or then (13,4) semimetallic tube. The I-V measurements then suggests that this tube could also be a semimetallic one. However, more transport measurements would still be needed to carry out in order to

get reliable information about the band gaps. For genuine semiconducting tubes the Raman measurements gave several possibilities for chiral indices. The summary of all measured tubes is given in table 6.1.

One noticeable issue was that the diameter of the tube measured with AFM systematicly gave larger values than diameter deduced from RBM data. The reason for that could be that there is a systematic error in the AFM scanner and it should be calibrated properly. There is also one exception for that in tube A where the RBM diameter is actually larger than AFM diameter. The AFM image was taken near the electrode in quite poor spot having an additional dirt such resist from the electron beam lithography process also nearby. This can naturally diminish the diameter.

More detailed measurements need to be carried out in the future in order to investigate for example the band gaps and chiral index assignments of the tubes. One promising way to try to characterise the CNT is to perform electrical transport, Raman and TEM measurements on the same tube. This can be done for the samples that are fabricated as described in section 4.2. Also SNOM measurements combined with electrical transport measurements would give useful and more detailed information about CNTs.

Bibliography

[1] Reibold M., Paufler P., Levin A. A., Kochmann W., Pätzke N., Meyer D. C., *Carbon nanotubes in an ancient Damascus sabre*, Nature Vol. 444, 286 (2006)

[2] Radushkevich L. V., Lukyanovich V. M., *O strukture ugleroda, obrazujucegosja pri termiceskom razlozenii okisi ugleroda na zeleznom kontakte*. Soviet Journal of Physical Chemistry, Vol. 26, 88-95, (1952)

[3] Oberling A., Endo M., Koyama T., *Filamentous growth of carbon through benzene decomposition*, Journal of Crystal Growth, Vol. 32, 335-349 (1976)

[4] Kroto H. W., Heath J. R., O'Brien S. C., Curl R. F., Smalley R. E., *C_{60}: Buckminsterfullerene*, Nature, Vol. 318, 162-163 (1985)

[5] Iijima S., *Helical microtubules of graphitic carbon*, Nature, Vol. 354, 56-58 (1991)

[6] Iijima S., Ichihashi T., *Single-shell carbon nanotubes of 1-nm diameter*, Nature, Vol. 363, 603-605 (1993)

[7] Bethune D. S., Klang C. H., de Vries M. S., Gorman G., Savoy R., Vazquez J., Beyers R., *Cobalt-catalysed growth of carbon nanotubes with single-atomic-layer walls*, Nature, Vol. 363, 605-607 (1993)

[8] Novoselov K. S., Geim A. K., Morozov S. V., Jiang D., Zhang Y., Dubonos S. V., Grigorieva I. V., Firsov A. A., *Electric Field Effect in Atomically Thin Carbon Films*, Science, Vol. 306, 666-669 (2004)

[9] Geim A. K., Novoselov K. S., *The rise of graphene*, Nature materials, Vol. 6, 183-191 (2007)

[10] Jorio A., Dresselhaus G., Dresselhaus M. S. (Eds.), *Carbon Nanotubes*, Topics in Applied Physics, Vol.111, Springer-Verlag Berlin Heidelberg (2008)

[11] Saito R., Dresselhaus G., Dresselhaus M. S., *Physical properties of carbon nanotubes, first edition*, Imperial College Press, UK (1998)

[12] Rinkiö M., Johansson A., Zavodchikova M. Y., Toppari J. J., Nasibulin A. G., Kauppinen E. I., Törmä P., *High-yield of memory elements from carbon nanotube field-effect transistors with atomic layer deposited gate dielectric*, New Journal of Physics, Vol. 10, 103019 (2008)

[13] Charlier J-C., Blase X., Roche S., *Electronic and transport properties of nanotubes*, Review of Modern Physics, Vol. 79, 677-732 (2007)

[14] Mintmire J. W., White C. T., *Universal Density of States for Carbon Nanotubes*, Physical Review Letters, Vol. 81, 2506-2509 (1998)

[15] Kittel C., *Introduction to Solid State Physics, seventh edition*, John Wiley & Sons, Inc., UK (1996)

[16] White C. T., Mintmire J. W., *Density of states reflects the diameter of nanotube*, Nature, Vol. 394, 29-30 (1998)

[17] Datta S., *Quantum Transport: Atom to Transistor, first edition*, Cambridge University Press, UK (2007)

[18] Datta S., *Electronic Transport in Mesoscopic Systems, first edition*, Cambridge University Press, UK (1997)

[19] Kong J., Yenilmez E., Tombler T. W., Kim W., Dai H., *Quantum Interference and Ballistic Transmission in Nanotube Electron Waveguides*, Physical Review Letters, Vol. 87, 106801 (2001)

[20] Mann D., Javey A., Kong J., Wang Q., Dai H., *Ballistic Transport in Metallic Nanotubes with Reliable Pd Ohmic Contacts*, Nano letters, Vol. 3, 1541-1544 (2003)

[21] Javey A., Guo J., Wang Q., Lundstrom M., Dai H., *Ballistic carbon nanotube field-effect transistors*, Nature, Vol. 424, 654-657 (2003)

[22] White C. T., Todorov T. N., *Carbon nanotubes as long ballistic conductors*, Nature, Vol. 393, 240-242 (1998)

[23] Heinze S., Tersoff R., Derycke V., Appenzeller J., Avouris P., *Carbon Nanotubes as Schottky Barrier Transistors*, Physical Review Letters, Vol. 89, 106801 (2002)

[24] Elliot S. R., *The Physics and Chemistry of Solids, first, corrected edition*, John Wiley & Sons Inc., UK (2005)

[25] Léonard F., Tersoff J., *Role of Fermi-Level Pinning in Nanotube Schottky Diodes*, Physical Review Letters, Vol. 84, 4693-4696 (2000)

[26] Dai H., Javey A., Pop E., Mann D., Kim W., Lu Y., *Electrical Transport Properties and Field Effect Transistors of Carbon Nanotubes*, NANO, Vol. 1, 1-13 (2006)

[27] Liu P., Sun Q., Zhu F., Liu K., Liu L., Li Q., Fan S., *Measuring the Work Function of Carbon Nanotubes with Thermionic Method*, Nano Letters, Vol. 8, 647-651 (2008)

[28] Chen Z., Appenzeller J., Knoch J., Lin Y., Avouris P., *The Role of Metal-Nanotube Contact in the Performance of Carbon Nanotube Field-Effect Transistors*, Nano Letters, Vol. 5, 1497-1502 (2005)

[29] Pop E., Mann D., Cao J., Wang Q., Goodson K., Dai H., *Negative Differential Conductance and Hot Phonons in Suspended Nanotube Molecular Wires*, Physical Review Letters, Vol. 95, 155505 (2005)

[30] Zhou X. J., Park J. Y., Huang S. M., Liu J., McEuen P. L., *Band structure, phonon scattering, and the performance limit of the single-walled carbon nanotube transistors*, Physical Review Letters, Vol. 95, 146805 (2005)

[31] Cómez-Navarro C., De Pablo P. J., Gmez-Herrero J., Biel B., Garcia-Vidal F. J., *Tuning the conductance of single-walled carbon nanotubes by ion irradiation in the Anderson localization regime*, Nature materials, Vol. 4, 534-539 (2005)

[32] Minot E. D., Yaish Y., Sazonova V., Park J-Y., Brink M., McEuen P. L., *Tuning Carbon Nanotube Band Gaps with Strain*, Physical Review Letters, Vol. 90, 156401 (2003)

[33] Postma H., Teepen T., Yao Z., Grifoni M., Dekker C., *Carbon Nanotube Single-electron Transistors at Room Temperature*, Science, Vol. 293, 76-79 (2001)

[34] Pureval M. S., Hong B. H., Ravi A., Chandra B., hone J., Kirn P., *Scaling of Resistance and Electron Mean Free Path of Single-Walled Carbon Nanotubes*, Physical Review Letters, Vol. 98, 186808 (2007)

[35] Kuzmany H., Atkinson K., Mehring M., Roth S. (Eds.), *Electronic Properties of Molecular Nanostructures: XV International Winterschool/Euroconference*, AIP Conference Proceedings, Vol. 591, 401-404 (2001)

[36] Liang W., Bockrath M., Bozovic D., Hafner J. H., Tinkham M., Park H., *Fabry-Prot interference in a nanotube electron waveguide*, Nature, Vol. 411, 665-669 (2001)

[37] Kohn W., *Image of the Fermi surface in the vibration spectrum of metal*, Physical Review Letters, Vol. 2, 393-394 (1959)

[38] Samsonidze Ge. G., Barros E. B., Saito R., Jiang J., Dresselhaus G., Dresselhaus M. S., *Electron-phonon coupling mechanism in two-dimensional graphite and single-wall carbon nanotubes*, Physical Review B, Vol. 75, 155420 (2007)

[39] Piscanec S. Lazzeri M., Robertson J., Ferrari A. C., Mauri F., *Optical phonons in carbon nanotubes: Kohn anomalies, Peierls distortions, and dynamic effects*, Physical Review B, Vol. 75, 035427 (2007)

[40] Piscanec S., Lazzeri M., Mauri F., Ferrari A. C., *Optical phonons of graphene and nanotubes*, European Physical Journal Special Topics, Vol. 148, 159-170 (2007)

[41] Piscanec S., Lazzeri M., Mauri F., Ferrari A. C., Robertson J., *Kohn Anomalies and Electron-Phonon Interactions in Graphite*, Physical Review Letters, Vol. 93, 185503 (2004)

[42] Boyd R. W., *Nonlinear Optics, second edition*, Academic Press, UK (2003)

[43] Ferraro J. R., Nakamoto K., Brown, C. W., *Introductory raman spectroscopy, second edition*, Academic Press, UK (2003).

[44] Barros E. B., Jorio A., Samsonidze Ge. G., Capaz R. B., Souza Filho A. G., Filho J. M., Dresselhaus G., Dresselhaus M. S., *Review of symmetry-related properties of carbon nanotubes*, Physics Reports, Vol. 431, 261-302 (2006)

[45] Maultzsch J., Telg H., Reich S., Thomsen C., *Radial breathing mode of single-walled carbon nanotubes: Optical transition energies and chiral-index assignment*, Physical Review B, Vol. 72, 205438 (2005)

[46] Dresselhaus M. S., Dresselhaus G., Jorio A., Souza Filho A. G., Saito R., *Raman spectroscopy on isolated single wall carbon nanotubes*, Carbon, Vol. 40, 2043-2061 (2002)

[47] Saito R., Samsonidze Ge. G., Brar V. W., Dresselhaus G., Dresselhaus M. S., Jorio A., Cancado L. G., Fantini C., Pimenta M. A., Souza Filho A. G., *Double resonance Raman spectroscopy of single-wall carbon nanotubes*, New Journal of Physics, Vol. 5, 1-15 (2003)

[48] Pimenta M. A., Hanlon E. B., Marucci A., Corio P., Brown S. D. M., Empedocles S. A., Bawendi M. G., Dresselhaus G., Dresselhaus M. S., *The anomalous dispersion of the disorder-induced and the second-order Raman bands*, Brazilian Journal of Physics, Vol. 30, 423-427 (2000)

[49] Pimenta M. A., Jorio A., Brown S. D. M., Souza Filho A. G., Dresselhaus G., Hafner J. H., Lieber C. M., Saito R., Dresselhaus M. S., *Diameter dependence of the Raman D-band in isolated single-wall carbon nanotube*, Physical Review B, Vol. 64, 041401 (2000)

[50] Souza M., Jorio A., Fantini C., Neves B. R. A., Pimenta M. A., Saito R., Ismach A., Joselevich E., Brar V. W., Samsonidze Ge. G., Dresselhaus G, Dresselhaus

M.S., *Single- and double-resonance Raman G-band processes in carbon nanotubes*, Physical Review B, Vol. 69, 241403 (2004)

[51] Brown S. D. M., Jorio A., Corio P., Dresselhaus M. S., Dresselhaus G., Saito R., Kneipp K., *Origin of the Breit-Wigner-Fano lineshape of the tangential G-band feature of metallic carbon nanotubes*, Physical Review B, Vol. 63, 155414 (2001)

[52] Jiang C., Kempa K., Zhao J., Schlecht U., Kolb U., Basch T., Burghard M., Mews A., *Strong enhancement of the Breit-Wigner-Fano Raman line in carbon nanotube bundles caused by plasmon band formation*, Physical Review B, Vol. 66, 161404 (2002)

[53] Kempa K., *Gapless plasmons in carbon nanotubes and their interactions with phonons*, Physical Review B, Vol. 66, 195406 (2002)

[54] Paillet M., Poncharal Ph., Zahab A., Sauvajol J.-L., Meyer J. C., Roth S., *Vanishing of the Breit-Wigner-Fano Component in Individual Single-Wall Carbon Nanotubes*, Physical Review Letters, Vol. 94, 237401 (2005)

[55] Bose S. M., Gayen S., Behera S. N., *Theory of the tangential G-band feature in the Raman spectra of metallic carbon nanotubes*, Physical Review B, Vol. 72, 153402 (2005)

[56] Kataura H., Kumazawa Y., Maniwa Y., Umezu I., Suzuki S., Ohtsuka Y., Achiba Y., *Optical Properties of Single-Wall Carbon Nanotubes*, Synthetic metals, Vol. 103, 2555-2558 (1999)

[57] Hartschuh A., Sánchez E. J., Xie X. S., Novotny L., *High-Resolution Near-Field Raman Microscopy of Single-Walled Carbon Nanotubes*, Physical Review Letters, Vol. 90, 095503 (2003)

[58] `http://www.nanocyl.com/products/research/1100.php` (read on 8.11.2008)

[59] Nagy J. B., Bister G., Fonseca A., Mehn D., Konya Z., Kiricsi I., Horvath Z. E., Biro L. P., *On the growth mechanism of single-walled carbon nanotubes by catalytic carbon vapor deposition on supported metal catalysts*, Journal of Nanoscience and Nanotechnology, Vol. 4, 326-345 (2004)

[60] Nasibulin, A. G., Moisala, A., Brown, D. P., Jiang, H., Kauppinen, E. I., *A novel aerosol method for single walled carbon nanotube synthesis*, Chemical Physics Letters, Vol. 402, 227-232 (2005)

[61] Seidel H., Csepregi L., Heuberger A., Baumgärtel H., *Anisotropic Etching of Crystalline Silicon in Alkaline Solutions*, J. Electrochem. Soc., Vol. 137, 3612-3632 (1990)

[62] Makarovski A., Zhukov A., Liu J., Finkelstein G., *Four-probe measurements of carbon nanotubes with narrow metal contacts*, Physical Review B, Vol. 76, 161405R (2007)

[63] Ferry D. K., Goodnick S. M., *Transport in Nanostructures, first edition*, Cambridge University Press, UK (1999)

[64] Bockrath M., Cobden D. H., McEuen P. L., Chopra N. G., Zettl A., Thess A., Smalley R. E., *Single-Electron Transport in Ropes of Carbon Nanotubes*, Science, Vol. 275, 1922-1925 (1997)

[65] Radosavljevi M., Freitag M., Thadani K. V., Johnson A. T., *Nonvolatile Molecular Memory Elements Based on Ambipolar Nanotube Field Effect Transistors*, Nano Letters, Vol. 2, 761-764 (2002)

[66] Kuroda M. A., Leburton J-P., *Joule heating induced negative differential resistance in freestanding metallic carbon nanotubes*, Applied Physics Letters, Vol. 89, 103102 (2006)

[67] Léonard F., Tersoff J., *Negative Differential Resistance in Nanotube Devices*, Physical Review Letters, Vol. 85, 4768-4770 (2000)

[68] Léonard F., Tersoff J., *Multiple Functionality in Nanotube Transistors*, Physical Review Letters, Vol. 88, 258302 (2002)

[69] Araujo P. T., Doorn S. K., Kilina S., Tretiak S., Einarsson E., Maruyama S., Chacham H., Pimenta M. A., Jorio A., *Third and Fourth Optical Transitions in Semiconducting Carbon Nanotubes*, Physical Review Letters, Vol. 98, 067401 (2007)